CCFE
CULHAM CENTRE FOR FUSION ENERGY

UK Atomic Energy Authority

UKAEA-CCFE-PR(18)13

S. Breton, F. J. Casson, C. Bourdelle, J. Citrin, Y. Baranov, Y. Camenen, C. Challis, J. Garcia, G. Corrigan, L. Garzotti, S. Henderson, F. Koechl, M. OMullane, T. Pütterich, M. Sertoli, M. Valisa and the JET contributors

First principle integrated modeling of multi-channel transport including Tungsten in JET

First principle integrated modeling of multi-channel transport including Tungsten in JET

S. Breton,[1] F. J. Casson,[2] C. Bourdelle,[1] J. Citrin,[3] Y. Baranov,[2] Y. Camenen,[4] C. Challis,[2] J. Garcia,[1] G. Corrigan,[2] L. Garzotti,[2] S. Henderson,[5] F. Koechl,[6] M. OMullane,[5] T. Pütterich,[7] M. Sertoli,[2] M. Valisa[8] and the JET contributors[9]

[1]*CEA, IRFM, F-13108 Saint-Paul-lez-Durance, France*

[2]*CCFE, Culham Science Centre, Abingdon, Oxon, OX14 3DB, UK*

[3]*DIFFER - Dutch Institute for Fundamental Energy Research, Eindhoven, the Netherlands*

[4]*Aix-Marseille Université, CNRS, PIIM UMR 7345, 13397 Marseille Cedex 20, France*

[5]*Department of Physics SUPA, University of Strathclyde, Glasgow, G4 0NG, UK*

[6]*Association EURATOM-OAW/ATI, Atominstitut, TU Wien, 1020 Vienna, Austria*

[7]*Max-Planck-Institut für Plasmaphysik, Garching, Germany*

[8]*National Research Council Piazzale Aldo Moro, 7 - 00185, Roma, Italia*

[9]*See the author list of Overview of the JET results in support to ITER by X. Litaudon et al. to be published in Nuclear Fusion Special issue: overview and summary reports from the 26th Fusion Energy Conference (Kyoto, Japan, 1722 October 2016)*

This is a preprint of a paper submitted for publication in Nuclear Fusion

First principle integrated modeling of multi-channel transport including Tungsten in JET

S. Breton[1], F.J. Casson[2], C. Bourdelle[1], J. Citrin[3], Y. Baranov[2], Y. Camenen[4], C. Challis[2], J. Garcia[1], G. Corrigan[2], L. Garzotti[2], S. Henderson[5], F. Koechl[6], M. OMullane[5], T. Pütterich[7], M. Sertoli[2], M. Valisa[8], the JET contributors*

* EUROfusion Consortium, JET, Culham Science Centre, Abingdon, OX14 3DB, UK
[1] CEA, IRFM, F-13108 Saint-Paul-lez-Durance, France
[2] CCFE, Culham Science Centre, Abingdon, Oxon, OX14 3DB, UK
[3] DIFFER - Dutch Institute for Fundamental Energy Research, Eindhoven, the Netherlands
[4] Aix-Marseille Universit, CNRS, PIIM UMR 7345, 13397 Marseille Cedex 20, France
[5] Department of Physics SUPA, University of Strathclyde, Glasgow, G4 0NG, UK
[6] Association EURATOM-OAW/ATI, Atominstitut, TU Wien, 1020 Vienna, Austria
[7] Max-Planck-Institut fr Plasmaphysik, Garching, Germany
[8] National Research Council Piazzale Aldo Moro, 7 - 00185, Roma, Italia
* See the author list of Overview of the JET results in support to ITER by X. Litaudon et al. to be published in Nuclear Fusion Special issue: overview and summary reports from the 26th Fusion Energy Conference (Kyoto, Japan, 1722 October 2016)

Abstract. For the first time, over five confinement times, the self-consistent flux driven time evolution of heat, momentum transport and particle fluxes of electrons and multiple ions including Tungsten (W) is modeled within the integrated modeling platform JETTO [Romanelli M et al PFR 2014], using first principle-based codes : namely, QuaLiKiz [Bourdelle C. et al. PPCF 2016] for turbulent transport and NEO [Belli E A and Candy J PPCF 2008] for neoclassical transport. For a JET-ILW pulse, the evolution of measured temperatures, rotation and density profiles are successfully predicted and the observed W accumulation is obtained. The poloidal asymmetries of the W density modfying its neoclassical and turbulent transport are accounted for. Actuators of the W accumulation are studied : removing the central particle source annihilates the central W accumulation whereas the suppression of the torque reduces significantly the W central accumulation. Finally, the presence of W slightly reduces main ion heat turbulent transport through complex nonlinear interplays involving radiation, main ion dilution and collisionality.

1. Introduction

High-Z metallic materials, such as Tungsten (W), are chosen for their high melting point, low erosion rate and low hydrogen retention. W will be used in ITER on the divertor tiles [1]. But due to its large charge number 74, W ions are not fully ionized

even in the hot tokamak core, leading to an important level of line radiation. This means that W accumulation in the plasma core can be highly deleterious. To avoid central W accumulation, an accurate understanding of W transport is a key issue. In the central region of JET core, W transport has been shown to be mostly caused by neoclassical convection [2, 3, 4, 5, 6], whereas in the outer part the turbulent diffusion dominates. Neoclassical transport depends on main ion temperature and density gradients, as well as on plasma rotation. Therefore, in order to understand the mechanisms of W transport, it is crucial to predict accurately and self-consistently the time evolution of the temperature, density and rotation profiles. To do so, one needs to model the interplay between heat, angular momentum and particle, accounting for sources, losses and transport (both neoclassical and turbulent), over multiple confinement times while self-consistently modelling the current diffusion. Therefore the use of an integrated modeling tool such as JETTO [7] is mandatory.

The goal of this work is to reproduce the experimental behavior of an extensively studied JET-ILW hybrid H mode (#82722) over 5 confinement times, i.e. 1.7 s. While it has been demonstrated that MHD phenomena impact the W behavior in the core through sawteeth [8] and at the edge through Edge Localized Modes [9], they are not modeled in our simulations. This decision is based on the results of [6], where, at given times, the W turbulent transport modeled by GKW [10] and the W neoclassical transport modeled by NEO [11, 12] successfully reproduce the 2D W density profile. Therefore, in our JETTO integratted modelling, the neoclassical transport is modelled using NEO and the turbulent transport using QuaLiKiz [13, 14, 15]. Due its too expensive CPU cost, GKW even in its quasilinear version cannot be integrated in JETTO, therefore QuaLiKiz is used instead. QuaLiKiz is a quasilinear gyrokinetic code which has been widely validated against other quasilinear and nonlinear gyrokinetic codes [14]. The initial W content was adjusted to match the initial bolometry signal. The W boundary condition at the Last Closed Flux Surface (LCFS) was a constant incoming flux. The transport is the pedestal was fixed during the simulation with adjusted transport coefficients matching ELM-averaged electron density and temperature measurements. With these settings, the JETTO-NEO-QuaLiKiz modelling of the JET-ILW pulse #82722 over 5 confinement times, i.e. 1.7 s, reproduced succesfully and simultenaously the electron and ion temperatures, the electron density, the toroidal rotation profiles as well as the 2D W profiles.

Thanks to this successful multi-channels, multi confinement times, flux driven simulation, the W accumulation actuators could be identified. The W core accumulation was completely mitigated by removing the central NBI particle source. Removing the NBI torque allowed to reduce significantly the W accumulation. Showing that tokamaks with lower core fuelling and lower torque input such as WEST or ITER should be less prone to core W accumulation. Finally, the W presence was shown to lead to an improved heat confinement through complex non-linear interplays invoking modified T_e/T_i due to modified radiation losses, modified dillution and collisionality, all impacting the turbulent transport.

In section 2, the studied JET-ILW pulse is presented. In section 3, the JETTO-NEO-QuaLiKiz configuration used in this work is reviewed. In section 4, the predicted profiles by JETTO-NEO-QuaLiKiz are compared to the measured ones. Section 5 focuses on two actuators leading to W accumulation : NBI central particle source and NBI torque. Section 6 explains the mechanisms at play behind the W stabilization effect. Finally, conclusions are drawn in section 7

2. JET-ILW plasma profiles and W accumulation phenomenon

Understanding and modeling the mechanisms leading to central W accumulation is a key issue. In this perspective, [6] presents a detailed analysis of the hybrid JET-ILW shot #82722. For two time slices, JETTO [7]-SANCO [16] interpretive simulations are run, with density, temperature and rotation profiles made of fits from experimental data.

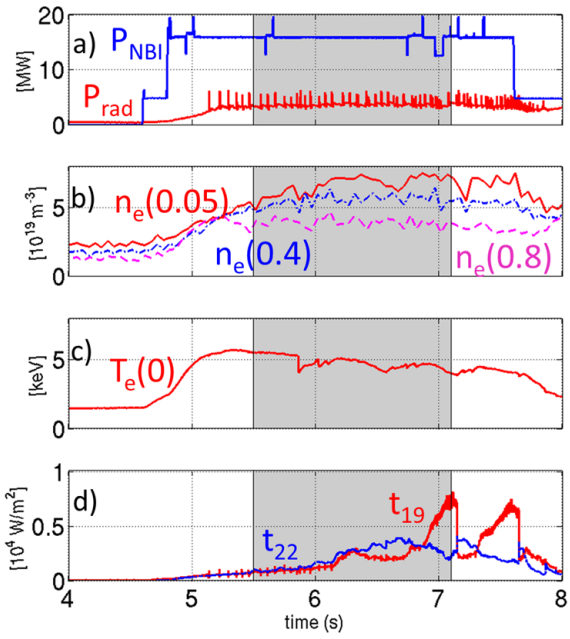

Figure 1: Experimental time traces of NBI and radiated power from bolometry (a), electron density at different position from HRTS (b), central electron temperature from ECE (c), and central (t19) and ρ=0.22 (t22) SXR lines of 82722 JET pulse

Time traces of the chosen JET-ILW pulse (#82722 B_T=2T I_P=1.7MA) are shown on figure 1. The modeled time window corresponds to the shaded area, from 5.5s to 7.1s. In this time window, Neutral Beam Injection (NBI) at 16 MW is the only auxiliary heating. The presence of ELMs in the pedestal is visible on the total radiated power on 1a. The SXR central line t_{19} on figure 1d shows strong peakings when compared with the peripheric SXR line t_{22}, which indicates the W central accumulation, visible also on figure 3. Around 5s, the electron density shown on 1b has a hollow profile, which

is more visible on figure 2a. Then the central density peaks, though limited by three sawtooth crashes at 5.9s, 6.5s and 7.1s, with an inversion radius at $\rho \approx 0.25$, where ρ is the square root of the normalized toroidal flux. The sawteeth can also be seen on the central temperature on 1c and on the central SXR line on 1d. The central electron temperature on 1c first increases until 5.5s, then tends to decrease with time. Note that there is no SXR peak corresponding to the time between the sawteeth at 5.9s and 6.5s. It comes from the fact that W has not yet moved towards the axis, as seen later of figure 3a.

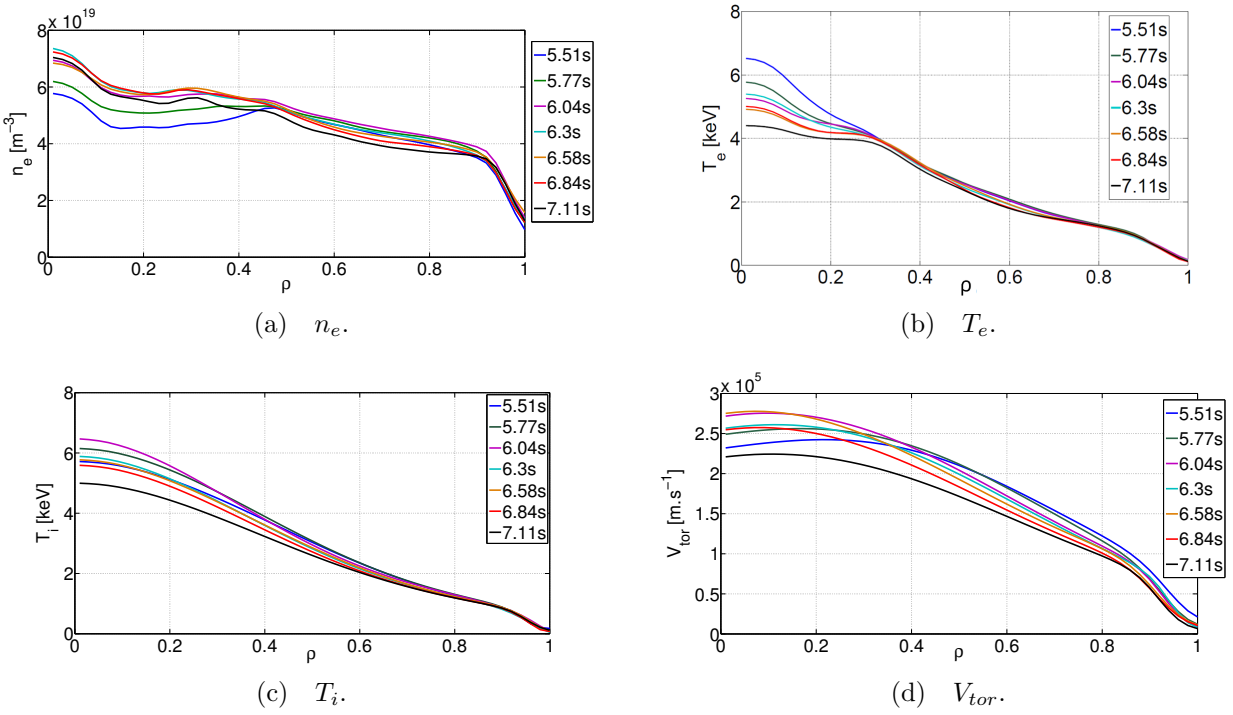

(a) n_e. (b) T_e.

(c) T_i. (d) V_{tor}.

Figure 2: (a) electron density profiles, (b) electron temperature profiles, (c) ion temperature profiles, (d) toroidal rotation profiles. Obtained by cubic spline fits of the JET HRTS and Charge Exchange diagnostics plotted against ρ at various times

Selection of electron density and temperature profiles obtained by cubic spline fits of the JET High Resolution Thomson Scattering (HRTS, time resolution of 50 ms) diagnostic are presented on figure 2a and 2b. Note that the HRTS covers the axis. Through the whole time window, the pedestal height of the electron density fluctuates due to the presence of ELMs occuring at a frequency around 40Hz, visible on the radiation on figure 1. At the beginning of our time window, the electron density profile is hollow at 5.5s, which means that the density at ρ=0.2 is lower than the density around mid-radius. The central density is already peaked. This phenomenon is most likely caused by NBI central particle source (see figure 18a) and low central diffusivity [17]. Then the density builds up over time from mid-radius inward, keeping a strong central peaking. One sawtooth crash occurs between 6.3s and 6.5s, causing the central density

to drop. Between 6.8s and 7.1s the central density increases and then slightly drops again. As explained later on section 4, the density gradients, especially the central one, play a major role in W transport and accumulation.

On figure 2b, the electron temperature profiles remain quite unchanged from ρ=0.3 outward. The central temperature tends to decrease over time, from ρ=0.3 inward. The impact of the three sawtooth crashes (5.9s, 6.5s and 7.1s) is visible : the central temperature increases between 6s and 6.3s, and again between 6.6s and 6.8s. Overall, the central electron temperature drops by 35% in 1.6s.

On figure 2c, the ion temperature profiles also undergoes the sawtooth crashes since the central temperature increases between 6s and 6.3s, but the inversion radius is less visible. Finally, the rotation profiles on figure 2c behave quite similarly to the ion temperature profiles with the increase/decrease due to the sawteeth. Note that the toroidal rotation is quite large, between 2.10^5 and $3.10^5 m.s^{-1}$, which leads to W Mach number up to 3.

The poloidal cross sections of the W density are inferred from SXR-UV measurements extended to account for poloidal asymmetries [18]. They are shown on figure 3, at t=6.2s before the central SXR line on figure 1 peaks, and at t=7s during a SXR central line peak.

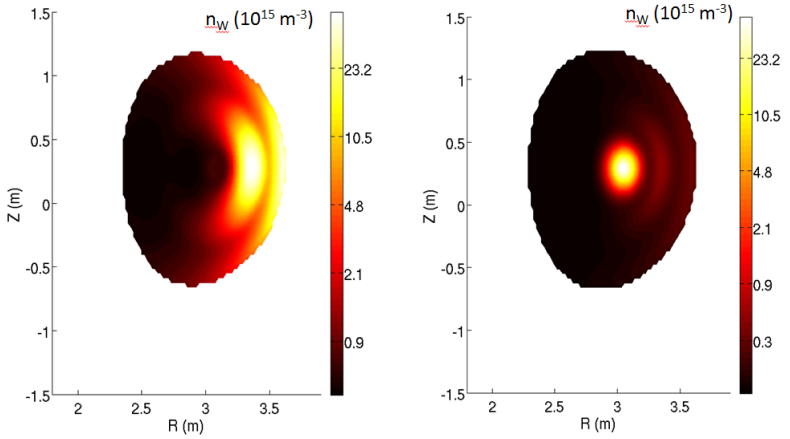

(a) 2D n_W at t=6.2s.

(b) 2D n_W at t=7s after 1.5s of simulation.

Figure 3: Poloidal cross sections of the W density inferred from SXR-UV measurements

On figure 3a at t=6.2s, the W did not reach the center yet and gathers at the Low Field Side, showing strong poloidal asymmetries as expected for rotating plasmas (see toroidal velocity profiles on figure 2d). At this time the W concentration on the Low Field Side (LFS) is around $n_W/n_D = 7.10^{-5}$ so the W is still a trace species, ie $\frac{Z_W^2 n_W}{Z_D^2 n_D} << 1$. At 7s shown on figure 3b a significant amount of W accumulated in the center of the plasma. The central W concentration reaches up $n_W/n_D = 4.10^{-3}$ therefore W is no longer a trace species.

The goal of this work is to model self-consistently the main features of the 82722 pulse : central electron density peaking, central electron temperature dropping, and W central accumulation by predicting with JETTO the time evolution of the plasma profiles (density, temperature, rotation) as well as the W profile.

3. JETTO configuration : codes, assumptions and numerical settings

The use of an integrated modeling tool is mandatory in order to evolve predictively many quantities at the same time : particles, heat, momentum as well as current and magnetic equilibrium. This section presents the JETTO configuration used for our specific case. Each code settings are briefly presented below, the corresponding numerical adjustments are shown in Appendix A.

JETTO is an integrated modelling plateform [19], where the heat, particle and angular momentum transport equations are solved over a chosen time period. Models for the sources are coupled to JETTO, as well as turbulent and neoclassical transport codes. In the JET pulse studied, only NBI is present, its associated heat, particle and angular momentum surces are modelled by PENCIL [20]. The turbulent transport in modelled by QuaLiKiz [14, 15] and the neoclassical transport by NEO [11, 12]. Our JETTO simulation evolves fully predictively, over several confinement times, seven channels : densities of main ion, W and Be, ion and electron temperatures, toroidal rotation, and current.

The time window, 5.5s to 7.1s, was chosen to be wide enough to cover several confinement times (with $\tau_E = \frac{W}{P_L}$ ≈0.3s with W total energy of the plasma and P_L the power loss) and at 7s the W already accumulated in the center (see figure 3b). The entire plasma radius is modeled within JETTO. The overall JETTO settings are detailed in the Appendix.

Figure 3a shows that W presents strong poloidal asymmetries, making the use of a code accounting for poloidal asymmetries such as NEO necessary. Within JETTO, NEO runs for the impurity neoclassical transport over the whole radius range, from the axis to the LCFS. For the turbulent transport, from $\rho = 0.03$ to pedestal top $\rho = 0.97$, the quasilinear gyrokinetic code QuaLiKiz is used. It is a first-principle quasilinear gyrokinetic code that accounts for trapped and passing ions and electrons, therefore Ion and Electron Temperature Gradients and Trapped Electron Modes. QuaLiKiz produces quasilinear gyrkinetic heat, particle and angular moement fluxes which have been successfully compared to non-linear gyrokinetic predictions [14, 21, 22]. In [15] the impact of poloidal asymmetries for turbulent transport of heavy impurities was also included. QuaLiKiz accounts for all unstable modes and sums the fluxes over the wave number spectrum. It uses the shifted circle (s-α) geometry with a small inverse aspect ratio expansion. Both QuaLiKiz and NEO codes are first-principle based and have a computational time compatible with integrated modelling (about 10 CPU seconds for a flux at a single radial location). Indeed, in JETTO, these transport codes are called at least 1000 times for each second of modelled tokamak plasma. More detailed NEO and

QuaLiKiz settings are given in the Appendix.

The pedestal region (ρ=0.97-1) is modeled using an "Edge Transport Barrier" (ETB), i.e. prescribed transport coefficients. The pedestal width and the turbulent transport remains fixed during the whole simulation. The code FRANTIC [23] models the neutral particle source at the LCFS. The transport coefficients and neutral particle source are tuned to reproduce the experimental T_e and n_e in this region within experimental uncertainties at all times. In the pedestal, the Prandtl number is also tuned to match the exprimental rotation. A continuous ELM model, with tuned particle diffusivity and thermal conductivity was also necessary to reproduce the experimental pedestal, as in [24]. More details on the ETB settings in JETTO are given in the Appendix.

The initial W density profile is fixed to be proportional to the electron density such that n_W/n_{Be} allows to match both the experimental value of $Z_{eff} = 1.34$, and the initial line integrated radiation level from bolometry diagnostic within 5% (3.27MW for experimental value of 3.41MW). Concerning the W boundary conditions, a constant W flux through the separatrix is fixed to 10^{15} part/s. Therefore, the incoming W is transported through the pedestal with the neoclassical transport coefficients.

Concerning the magnetic equilibrium, the separatrix is determined by EFIT [25] constraint by the measured kinetic pressure and the Faraday angles [26]. The current diffusion is self-consistently predicted in JETTO.

The impurity radiative losses, as well as the impurity density profiles are computed by SANCO [16]. SANCO runs for the whole radius range, treats all charge states of the impurities and returns the most probable one. The atomic data used for W is ADAS 50, based on [27]. ADAS96 is used for Be. The SANCO settings in JETTO are further detailed in the Appendix.

ELM crashes and sawteeth are not modeled in our specific case, although several models are available in JETTO/JINTRAC [24].

The heating source, in this case NBI only, is modeled using the PENCIL code [20]. PENCIL results were compared with NUBEAM in TRANSP [28] showing an agreement of the source profiles within 10%. PENCIL solves a simplified version of the Fokker-Planck equation and includes ionization by charge exchange, ionization by plasma electrons and ionization by plasma ions. PENCIL computes the NBI heat, particule and angular momentum sources. More details on the PENCIL seetings in JETTO are given in the Appendix.

In the following the above JETTO-SANCO-QuaLiKiz-NEO-PENCIL-FRANTIC-ETB settings will be run to solve the electron heat, ion heat, particle (D, W and Be) and angular momentum transport equations. In these equations, at each time step, the sources and the transport coefficients are recalculated, therefore they are evolved self-consistently over multiple time steps, at least 1000 per second, covering 5 confinement times (i.e. 1.7 s) of the JET H mode hybrid pulse #82722.

4. JETTO predictions versus experiments

In this section we compare the experimental measurements with the self-consistently predicted profiles for the JET-ILW shot #82722 between 5.5s and 7.1s using JETTO-SANCO-QuaLiKiz-NEO-PENCIL-FRANTIC-ETB settings detailed in the previous section and in the Appendix.

4.1. Timetraces of the plasma parameters

Figures 4 to 9 present timetraces of several plasma parameters which are self-consistently and simultaneously evolved in the simulation : density, temperature, rotation, current profiles as well as impurity content and radiation. For each parameter, the JETTO-SANCO-QuaLiKiz-NEO-PENCIL-FRANTIC-ETB simulation is shown in magenta, and compared with experimental measurements when available. Timetraces are shown at three ρ positions : 0.1, 0.4, and 0.75.

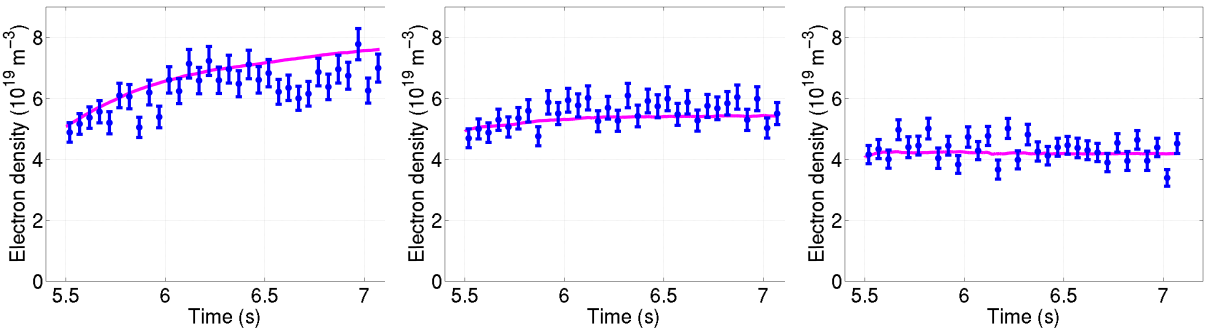

(a) ρ=0.1 (b) ρ=0.4 (c) ρ=0.75

Figure 4: Electron density timetraces : comparison between JETTO-SANCO-QuaLiKiz-NEO-PENCIL-FRANTIC-ETB prediction and HRTS measurements at different ρ

Figure 4 shows the time evolution of electron density. The density prediction must be accurate in order to simulate properly the W transport, due to the main ion density gradient dependence of the W neoclassical transport (see equation 2 of [29]). On figure 4a close to the center the predicted density increases smoothly. The HRTS measurements, while also globally increasing, are impacted by the sawteeth. The simulation does not take sawteeth into account, therefore the local gradients are not well captured at all times. For the two other radial positions, the predicted density does not vary much, and mostly stays within experimental uncertainties.

Figure 5 shows the electron temperature. Similarly to the electron density case, the simulation successfully captures the decreasing trend of central ECE measurements on figure 5a, but expectedly misses the sawtooth crashes. Around mid-radius (figure 5b) and close to the pedestal (figure 5c), the experimental temperature remains quite steady and the predictions lie within experimental uncertainties over time.

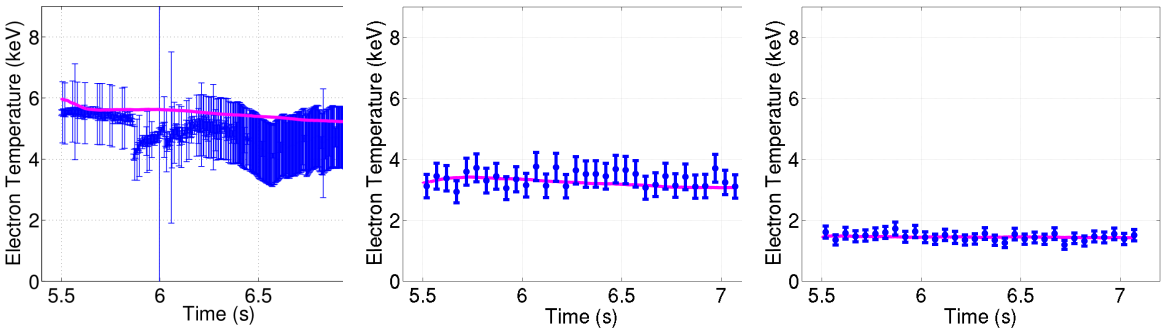

(a) ρ=0.1 (b) ρ=0.4 (c) ρ=0.75

Figure 5: Electron temperature timetraces : comparison between JETTO-SANCO-QuaLiKiz-NEO-PENCIL-FRANTIC-ETB prediction and ECE at $\rho = 0.1$/HRTS measurements at $\rho = 0.4 - 0.75$

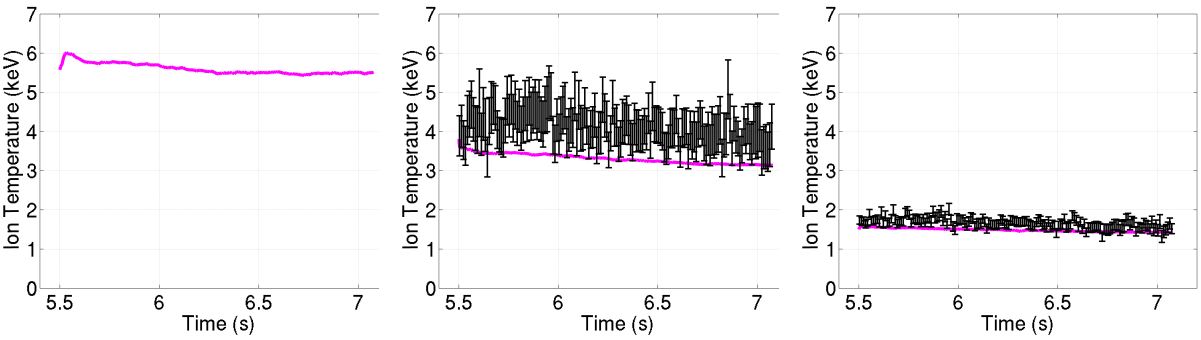

(a) ρ=0.1 (b) ρ=0.4 (c) ρ=0.75

Figure 6: Ion temperature timetraces : comparison between JETTO-SANCO-QuaLiKiz-NEO-PENCIL-FRANTIC-ETB prediction and Charge Exchange measurements at different ρ

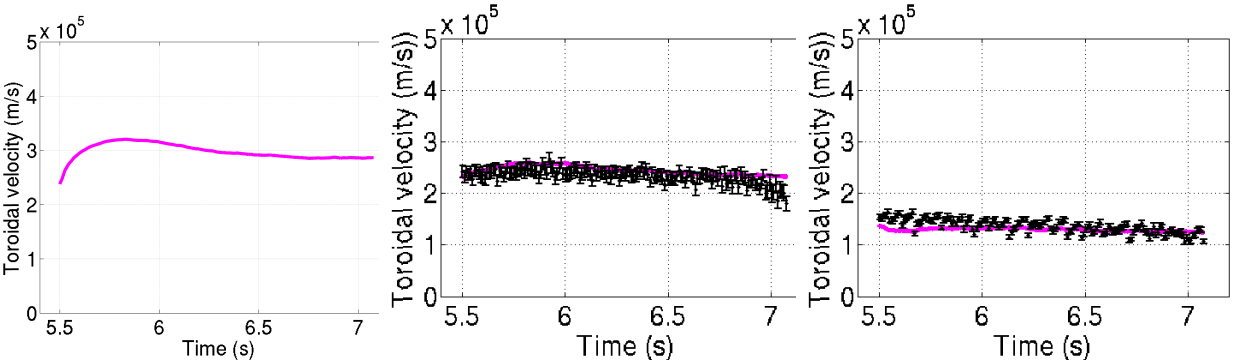

(a) ρ=0.1 (b) ρ=0.4 (c) ρ=0.75

Figure 7: Toroidal rotation timetraces : comparison between JETTO-SANCO-QuaLiKiz-NEO-PENCIL-FRANTIC-ETB prediction (magenta) and Charge Exchange measurements at different ρ

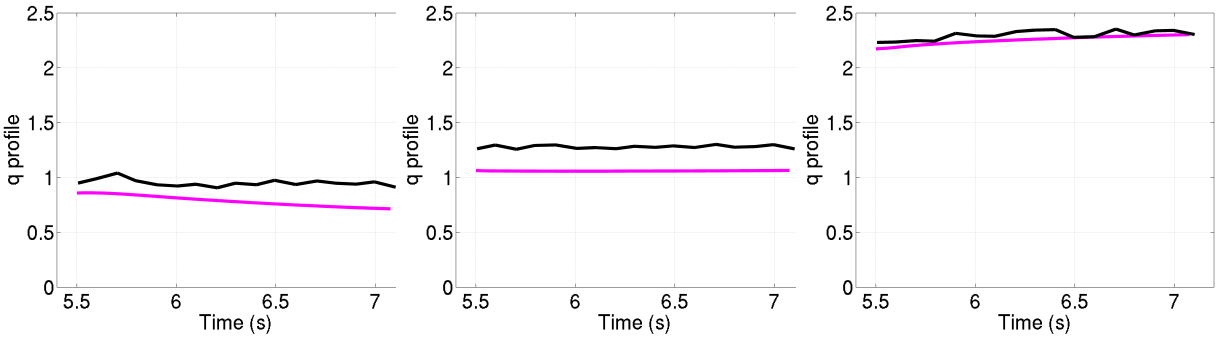

(a) ρ=0.1 (b) ρ=0.4 (c) ρ=0.75

Figure 8: Safety factor timetraces : comparison between JETTO-SANCO-QuaLiKiz-NEO-PENCIL-FRANTIC-ETB prediction (magenta) and EFIT reconstruction at different ρ

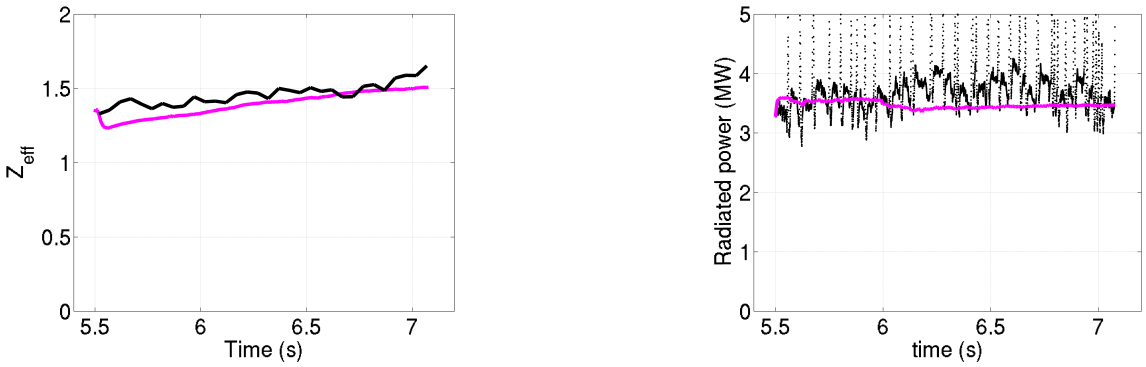

(a) Z_{eff} (b) Integrated radiation over time

Figure 9: Z_{eff} and radiation timetraces : comparison between JETTO-SANCO-QuaLiKiz-NEO-PENCIL-FRANTIC-ETB prediction (magenta) and measurements at different ρ

Ion temperature and toroidal rotation are not compared with experimental data in the center (figures 6a and 7a) due to lack of charge exchange data there. At $\rho = 0.4$ on figure 6b, the predictions tend to underestimate the charge exchange measurements by at most 15% (calculated from the lower bound of the error bar). This T_i underestimation can be explained by the fact that QuaLiKiz is an electrostatic code and does not account for nonlinear electromagnetic stabilization of ITG due to fast ions (see [15] and references therein).

Toroidal rotation predictions mostly lie within experimental uncertainties, except at early times at $\rho = 0.75$. Overall the experimental toroidal velocity remains quite constant over time. Note that the plasma rotates up to 30km/s, which leads to a W Mach number up to 3 leading to strong poloidal asymmetries.

The predictions of safety factor evolution are shown on figure 8. The self-consistent

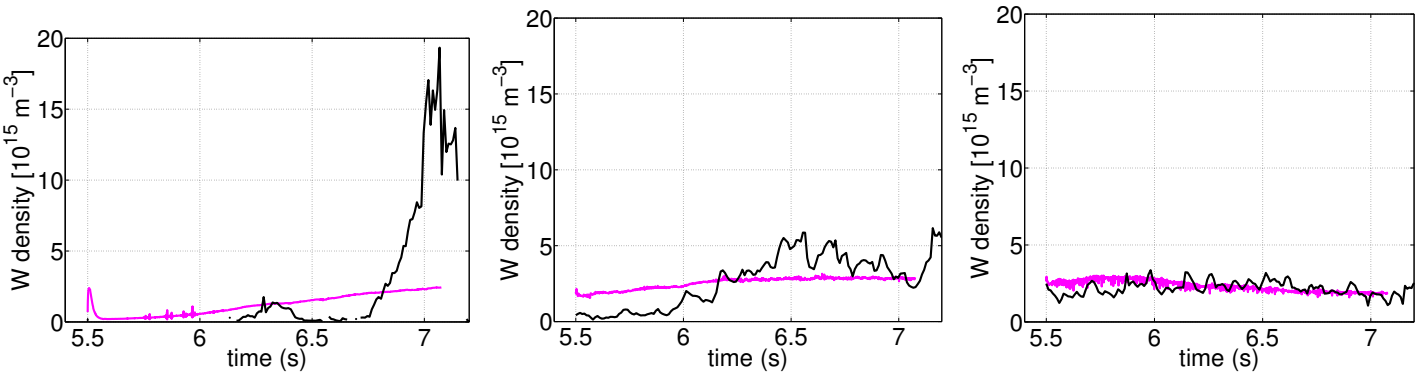

(a) ρ=0.05 (b) ρ=0.4 (c) ρ=0.8

Figure 10: W density timetraces : comparison between JETTO-SANCO-QuaLiKiz-NEO-PENCIL-FRANTIC-ETB prediction (magenta) and estimation from SXR-UV measurements at different ρ at $\theta = 0$. Simulation values renormalized to $< n_{W,sim}(0.4)/n_{W,exp}(0.4) >$

current diffusion equation solved in JETTO leads to these predictions of q. This predicted q differs slightly from the EFIT reconstruction constraint by kinetic pressure and Faraday angles [26].

Figure 9a shows the average Z_{eff} time evolution and figure 9b shows the total radiated power over time. The Z_{eff} globally increases with time, which can be explained by the fact that W contribution to Z_{eff} increases also with time. The line integrated radiated power does not increase over time, nor in the experiment neither in the simulation. The simulation does not account for ELMs, therefore it does not capture the regular bursts reported on the bolometer signal. The fact that the W accumulation is not visible on the line integrated bolometer signal is due to the fact that the W cooling factor is maximum around T=1.5 keV [27], hence off-axis for the pulse studied here.

Figure 10 shows the time evolution of the W content. The simulation values are renormalized to $< n_{W,sim}(0.4)/n_{W,exp}(0.4) >$, i.e the time average of the ratio of the simulation value over the measurement value at $\rho = 0.4$. The initial W content was estimated from the total radiation shown on figure 9b. Due to uncertainties, some experimental values are unavailable. In the very core, $\rho = 0.05$, the simulated W density slowly and regularly increases, with a factor 3 increase between 6s and 7s. The W density inferred from SXR-UV measurements [18] accumulates a little at 6.3s before being flushed out by the second sawtooth. Between the second and the third sawtooth, from 6.7s, the core W rises by a factor 10. The JETTO-SANCO-QuaLiKiz-NEO-PENCIL-FRANTIC-ETB simulation, which does not account for sawteeth, captures the core W accumulation. The predicted W content at $\rho = 0.4$ and $\rho = 0.8$ are compared to the measured ones in figures 10 (b) and (c).

To deepen the analysis of the quality of the JETTO-SANCO-QuaLiKiz-NEO-PENCIL-FRANTIC-ETB predictions, the next section focuses on several profiles at

different time slices, and 2D poloidal cuts of the W distribution.

4.2. Plasma profiles

4.2.1. Electron density In order to further validate QuaLiKiz predictions, figure 11 shows electron density profiles at three different times : 6.2s after 0.7s of simulation (figure 11a), 6.8s after 1.3s of simulation (figure 11b) and 7s, after 1.5s of simulation (figure 11c). Both HRTS and LIDAR are shown on figure 11 but we shall compare the simulation with HRTS only because of its higher time and space resolutions.

On figure 11a at 6.2s, QuaLiKiz predictions in magenta lie within experimental uncertainties of the HRTS in blue for the whole radius, except close to the axis where QuaLiKiz smoothes the local variations. The predicted pedestal is modeled by the ETB which has be tuned to match the experimental data. On figure 11b at 6.8s, QuaLiKiz prediction lies within experimental uncertainties from R=3.3m outward. But from R=3.3m inward, the experimental density dropped because of a sawtooth, therefore QuaLiKiz overestimates the central electron density. The experimental pedestal is stable and well captured by the Edge Transport Barrier modeling. On figure 11c at 7s after 1.5s of simulation, HRTS shows strong local gradients, especially close to the axis at R=3.1m. The experimental pedestal is slightly shifted outward, therefore the Edge Transport Barrier no longer lies within experimental uncertainties. QuaLiKiz captures the global increase of the electron density and lies within experimental uncertainties. However it does not really reproduces the stiff central gradient shown by the measurements and smooths it out. This impacts the W transport as seen in the next section.

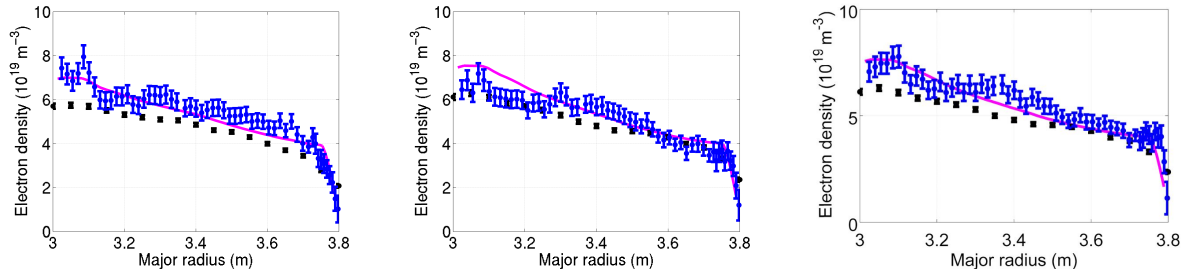

(a) Experimental and predicted n_e at t=6.2s after 0.7s of simulation.

(b) Experimental and predicted n_e at t=6.8s after 1.3s of simulation.

(c) Experimental and predicted n_e at t=7s after 1.5s of simulation.

Figure 11: Comparison of experimental (LIDAR in black HRTS in blue) and predicted (magenta solid line) electron density profiles

4.2.2. Electron and ion temperatures The electron and ion temperature predictions are then compared with experimental data. The electron temperature profiles are first shown on figure 12 : at 6.2s after 0.7s of simulation (figure 12a), at 6.8s after 1.3s

of simulation (figure 12b) and at 7s after 1.5s of simulation (figure 12c). QuaLiKiz predictions are in magenta solid line, and the HRTS measurements in blue.

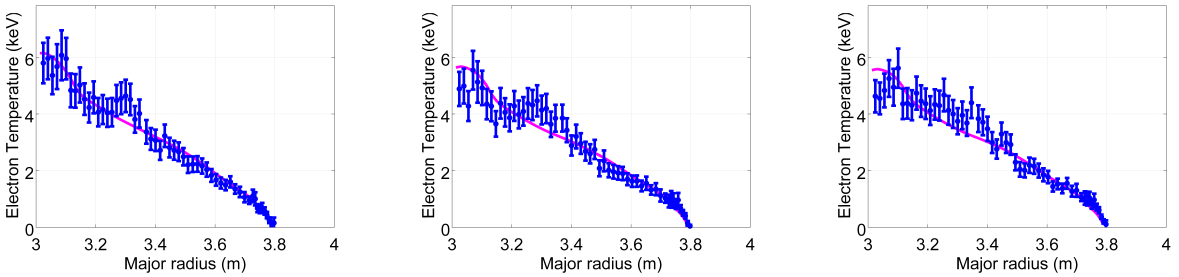

(a) Experimental and predicted T_e at t=6.2s after 0.7s of simulation.

(b) Experimental and predicted T_e at t=6.8s after 1.3s of simulation.

(c) Experimental and predicted T_e at t=7s after 1.5s of simulation.

Figure 12: Comparison of experimental (HRTS in blue) and predicted (magenta solid line) electron temperature profiles

On figure 12a at 6.2s, QuaLiKiz predictions of T_e in magenta lie within experimental uncertainties of the HRTS measurements in blue accross the whole radius, except at R=3.3m where QuaLiKiz misses a bump in T_e and slightly underestimates the measurements. On figure 12b at 6.8s, the HRTS shows a global decrease of the electron temperature, while keeping the central peaking and the bump at R=3.3m. The experimental pedestal remains unchanged and well reproduced by the Edge Transport Barrier. QuaLiKiz predicts the global decrease of the electron temperature, but still misses the bump at R=3.3m. QuaLiKiz predicts the central peaking and slightly overestimates it. On figure 12c at 7s after 1.5s of simulation, the bump at R=3.3m disappeared while a drop appeared at R=3.5m. QuaLiKiz predictions barely changed compared with 12b. Therefore it misses the drop at R=3.5m while staying within experimental uncertainties. QuaLiKiz still overestimates the very central temperature.

Now the ion temperature profiles are showed on figure 13 : at 6.2s after 0.7s of simulation (figure 13a), at 6.8s after 1.3s of simulation (figure 13b) and at 7s after 1.5s of simulation (figure 13c). QuaLiKiz predictions are in magenta solid line, and the Charge Exchange measurements are in black for most of the radial points, and blue for the pedestal.

On figure 13a at 6.2s, QuaLiKiz predictions in magenta lie within experimental uncertainties of the Charge Exchange for the whole radius. On figure 13b at 6.8s, the Charge Exchange shows a global increase of the ion temperature, up to 50% at R=3.2m. QuaLiKiz predictions remain almost unchanged and therefore underestimates the measurements by a maximum of 15% (calculated from the lower bound of the error bar). The possible reasons for this underestimations are already developed in the previous section. On figure 13c at 7s after 1.5s of simulation, measured ion temperature slightly decreased at R=3.25-3.4m. QuaLiKiz predictions barely changed compared with 13b. Therefore it still underestimates the measurements at R=3.25-3.4m.

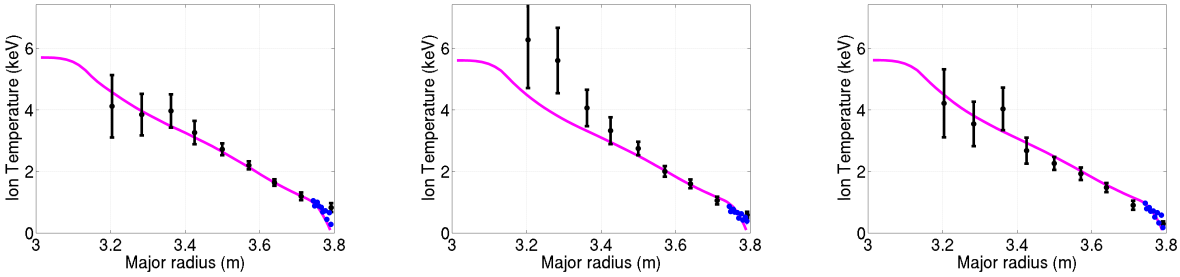

(a) Experimental and predicted T_i at t=6.2s after 0.7s of simulation.

(b) Experimental and predicted T_i at t=6.8s after 1.3s of simulation.

(c) Experimental and predicted T_i at t=7s after 1.5s of simulation.

Figure 13: Comparison of experimental (Charge exchange in dark) and predicted (magenta solid line) ion temperature profiles

4.2.3. Rotation The last plasma parameter to study is the toroidal rotation, shown on figure 14 : at 6.2s after 0.7s of simulation (figure 14a), at 6.8s after 1.3s of simulation (figure 14b) and at 7s after 1.5s of simulation (figure 14c). QuaLiKiz predictions are in magenta solid line, and the Charge Exchange measurements are in black for most of the radial points, and blue for the pedestal.

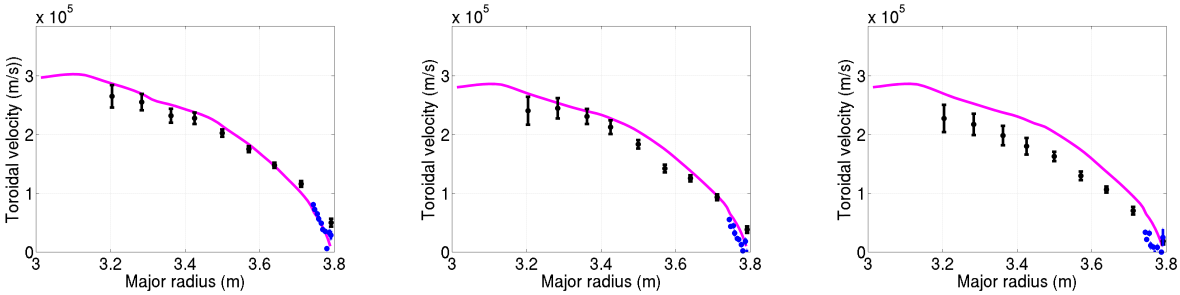

(a) Experimental and predicted V_{tor} at t=6.2s after 0.7s of simulation.

(b) Experimental and predicted V_{tor} at t=6.8s after 1.3s of simulation.

(c) Experimental and predicted V_{tor} at t=7s after 1.5s of simulation.

Figure 14: Comparison of experimental (Charge exchange in dark) and predicted (magenta solid line) toroidal rotation profiles

On figure 14a at 6.2s, QuaLiKiz predictions in magenta lie within experimental uncertainties of the Charge Exchange for the whole radius. The central part also lacks experimental measurements. On figure 14b at 6.8s, the Charge Exchange shows a slight global decrease of the toroidal rotation, especially at R=3.5-3.65m. QuaLiKiz predicts the global decreasing but overestimates the strongest decrease of the measurements at R=3.5-3.65m. Finally on figure 14c at 7s after 1.5s of simulation, measured velocity profile slightly smooths out and the pedestal moves slightly. QuaLiKiz predictions barely changed compared with 14b. Therefore it slightly overestimates the measurements at

R=3.3-3.7m and the Edge Transport Barrier model, which does not evolve, misses the pedestal.

4.3. W profiles and poloidal cuts

To analyze more precisely the time evolution of the W profile, figure 15 shows the Flux Surface Averaged W profiles at t=6.2s after 0.7s of simulation and t=7.1s after 1.6s of simulation. The experimental data is not available from $\rho = 0.7$ outwards where the SXR signal is too weak to constrain the W profile reocnstruction. Note that here, unlike for figure 10, the profiles are not renormalized one to the other.

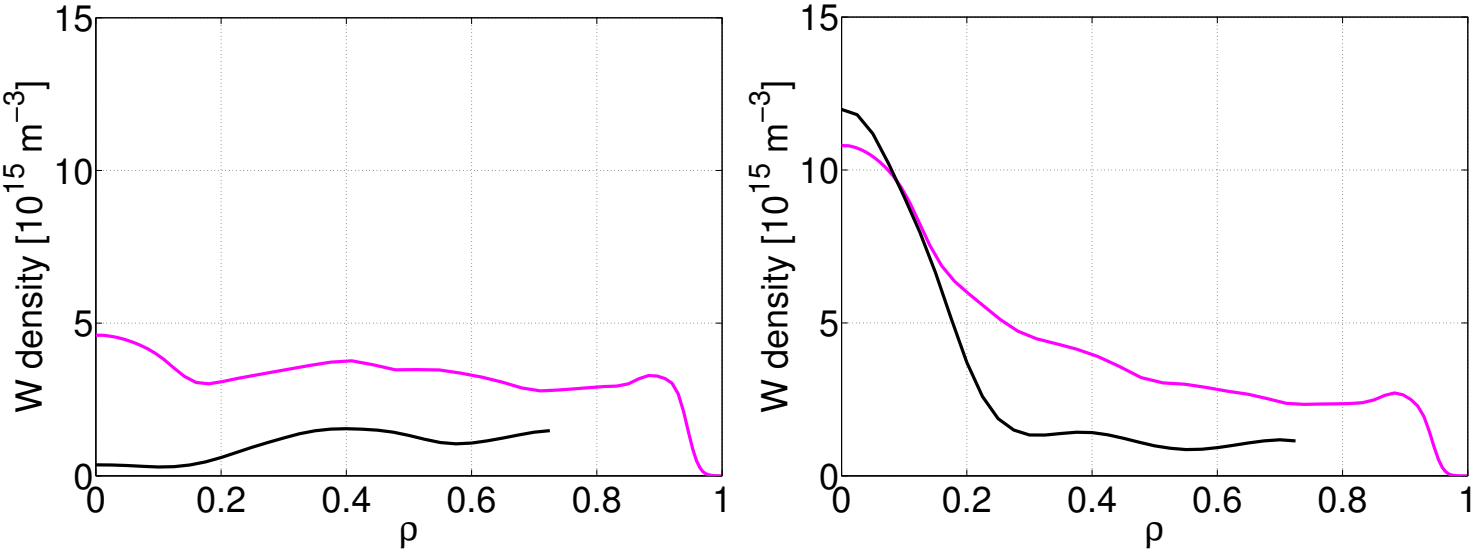

(a) n_W profile at t=6.2s after 0.7s of simulation.

(b) n_W profile at t=7.1s after 1.6s of simulation.

Figure 15: Comparison of profiles of estimated W density from SXR-UV measurements (black) and predicted W density (magenta) Flux Surface Averaged.

At 6.2s on figure 15a, the simulation over estimates the W content inferred from measurements by a factor 2 at mid-radius and up to a factor 10 in the very center where, according to the experimental data, the W did not migrate yet. This discrepancy probably comes from the initial condition which constraints the W profile to be homothetic to the electron density profile. At 7.1s, after 1.6 s, on figure 15b, the simulated central W content is very similar to the data inferred from SXR measurements, hence capturing the W core accumulation. The simulation still slightly overestimates the measurements from $\rho = 0.2$ outward.

Figures 16 and 17 below show 2D maps of the W density at three different times : t=6.2s after 0.7s of simulation and t=7s after 1.5s of simulation. W densities estimated from SXR-UV measurements are on the right, predictions are on the left.

On figure 16, one can see that the W density, both measured and simulated is in the $10^{15} m^{-3}$ range. The initial amount of W was homothetic to the electron density

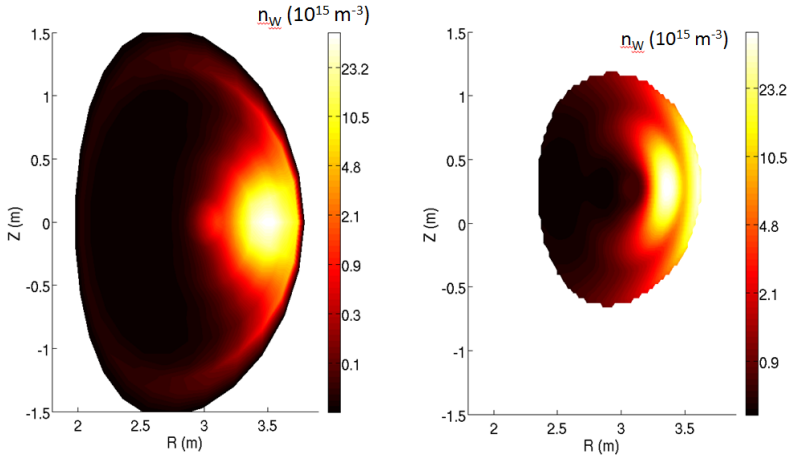

(a) Predicted n_W at t=6.2s after 0.7s of simulation.

(b) Experimental estimated n_W at t=6.2s.

Figure 16: Comparison of estimated W density from SXR-UV measurements (right) and predicted W density (left) at t=6.2s after 0.7s of simulation

profile, which is very different from experiment (see figure 15 (a)). Therefore in the simulated profiles there is W in the very core from the start, unlike the experiments. Concerning poloidal asymmetries, at 6.2s, both the measured and the simulated profiles show strong poloidal asymmetries, although they are weaker in the predicted profiles.

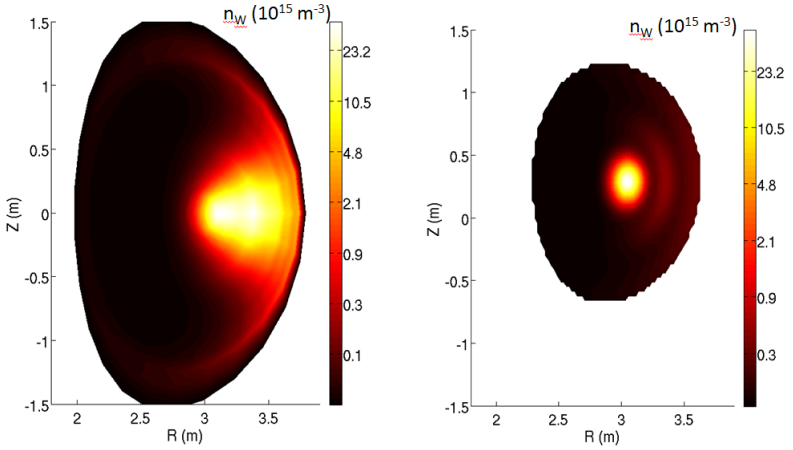

(a) Predicted n_W at t=7s after 1.5s of simulation.

(b) Experimental estimated n_W at t=7s after 1.5s of simulation.

Figure 17: Comparison of estimated W density from SXR-UV measurements (right) and predicted W density (left) at t=7s after 1.5s of simulation

At the end of the simulation, after 1.5s at t=7s, the estimation from measurements on figure 17b shows that most of the W moved towards the center and accumulated. On

the simulation, most of the W kept moving towards the center, but not fast enough and a significant W amount is still present at mid radius (see figure 10b and 10c). However the time evolution of the W behavior definitely shows a trend of core accumulation.

Three phenomena can explain why the simulation does not fully succeed in transporting all the W to the plasma center. The first explanation is that the simulation does not model sawteeth and therefore some transport mechanisms can be missed. The second explanation is that the initial W profile, with some W already in the center and at mid-radius unlike the experiment, remains present even after a few confinement times. The third explanation could be that QuaLiKiz, as seen on figure 11 globally captures the global central density peaking but does not fully reproduce all the local gradients, especially at mid-radius and in the center. This could lead to under estimated neoclassical transport and therefore a weaker central accumulation.

Overall, the accuracy of the QuaLiKiz predictions of the main plasma profiles, especially electron density and rotation, allows NEO and QuaLiKiz to correctly estimate the W neoclassical transport and therefore successfully reproduce the W central accumulation trend even though it does not capture all the experimental features.

5. Actuators leading to W accumulation

The simulation successfully predicts self-consistently and simultaneously the plasma profiles evolution, as well as the W tendency for central accumulation. In this section the actuators leading to the accumulation are studied. According to the equation of the neoclassical W flux from [29], two main physical parameters impact the W neoclassical flux: the density gradient and W poloidal asymmetries. Both can be modified through the NBI injection : the first one via the position of the NBI particle fuelling, the second is linked with the NBI angular momentum input.

5.1. Central particle fuelling

According to equation 2 of [29], the main ion gradient density has an unfavorable impact on the W neoclassical flux: the larger the density gradient, the larger the W convective flux. In the case of 82722, the particle fuelling is stronger in the central part (see figure 18a), causing the particle density to peak (figure 4a).

In order to confirm the link between central particle fuelling and central W accumulation, two new simulations are set : one with the particle injection artificially set to zero in PENCIL settings at all times; and the other with partial off-axis particle source at all times. In all cases, only the PENCIL NBI particle source is modified, the NBI heating and angular momentum input are kept identical to the original simulation. Figure 18a illustrates the NBI particle source profiles at 6.5s for the three cases.

Figure 18b shows the W density Flux Surface Averaged over time at ρ=0.05. The shaded section on figure 18b from t=5.5s to t=5.7s corresponds to the first simulated confinement time, needed for the simulation to move away from initial conditions.

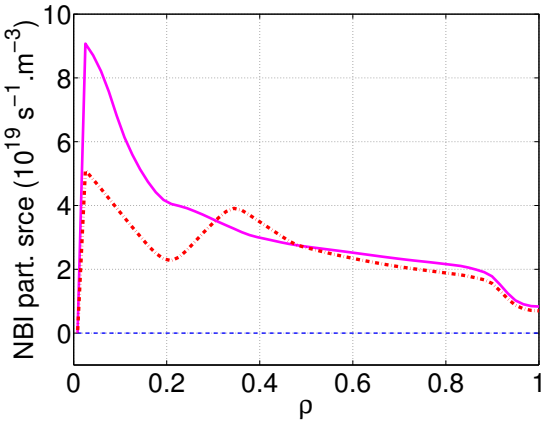

(a) NBI particle source profiles at t=6.5s, original 82722 settings in magenta, with the NBI particle source switched off in blue and with a particle source moved off-axis in red.

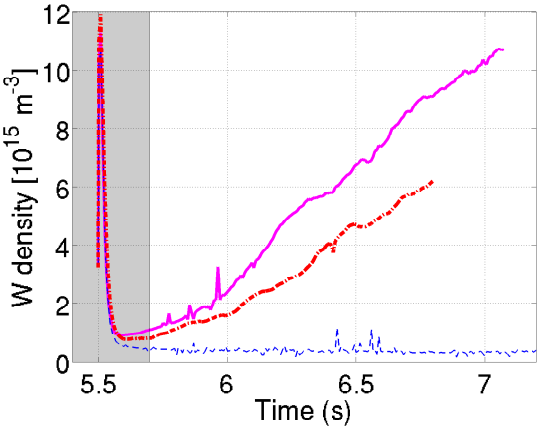

(b) W density Flux Surface Averaged at ρ=0.05 versus time.

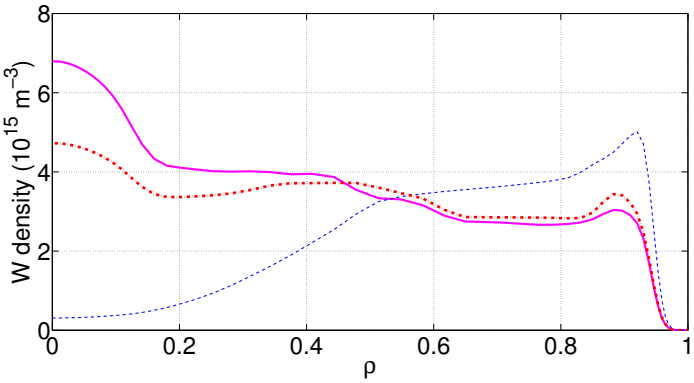

(c) W density Flux Surface Averaged profile at t=6.5s.

Figure 18: Study of the impact of central NBI particle source on W accumulation. Reference simulation (magenta), simulation with NBI particle source at zero (blue) and partial-off axis particle souce (red)

The removal of the central density source completely annihilates the W accumulation phenomenon. With a 45 % reduction of the central particle source, the central W density is reduced by 42%. Figure 18c shows the W density Flux Surface Averaged profile at t=6.5s. Without the central particle source, there is almost no W in the central part, most of the W is located in the outer half. The W density profiles of the reference simulation and the simulation with partial off-axis particle fuelling are quite similar from ρ=0.4-1, but in the center, the partial off-axis particle fuelling reduces the W central accumulation by 45%.

When switching off, or reducing the particle source, the background plasma profiles are impacted as well. This is illustrated on figure 19 for the density, temperatures and rotation profiles at t=6.5s. As expected, the removal on the central particle fuelling

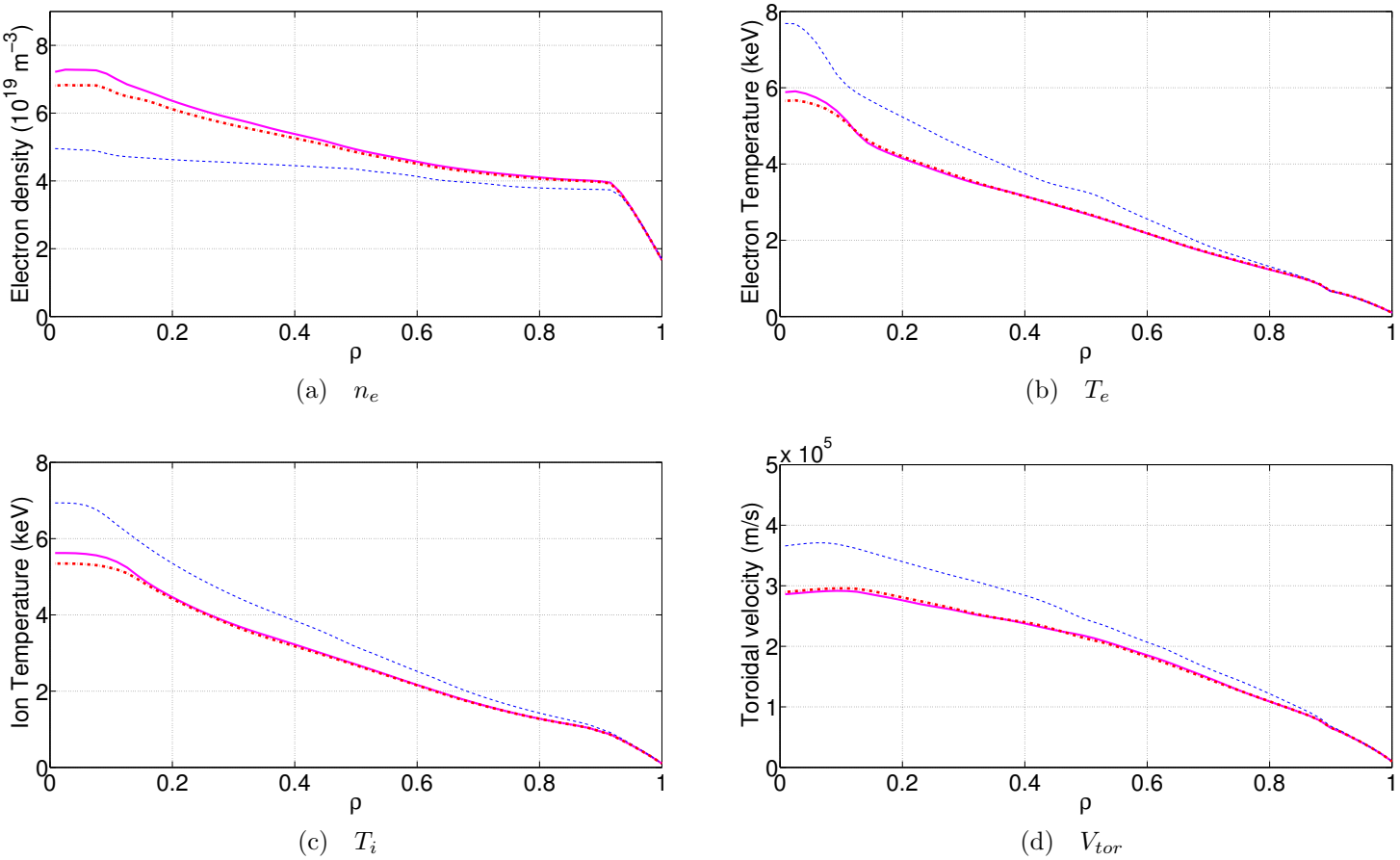

Figure 19: Density, temperatures and toroidal rotation profiles at t=6.5s. Reference simulation (magenta), no NBI particle source (blue), partially off-axis NBI particle source (red)

annihilates the central electron density peaking. The reduction of central fuelling by 45% in red leads to a reduction of the central density peaking by only 25%. Since without central particle fuelling, W does not accumulate, leading to larger temperatures in absence of core particle fuelling.

Overall this study demonstrates the deleterious correlation between NBI central particle fuelling and the W central accumulation. This is encouraging for devices such as WEST or ITER, with off-axis particle fuelling.

5.2. Toroidal rotation

The other parameter impacting significantly the W neoclassical transport is the rotation. The impact of poloidal asymmetries in the W neoclasscal transport is accounted for in the geometrical terms P_A and P_B terms in equation 2 of [29], and their range of appicability is studied in [30]. In this specific rotating JET-ILW pulse, these geometrical factors enhance the neoclassical convection up to a factor 40. In order to study the

impact of rotation on the W central accumulation, a simulation where the NBI angular momentum is set to zero while keeping identical the heat and particle sources. The resulting torque, and core W density evolution are illustrated on figure 20.

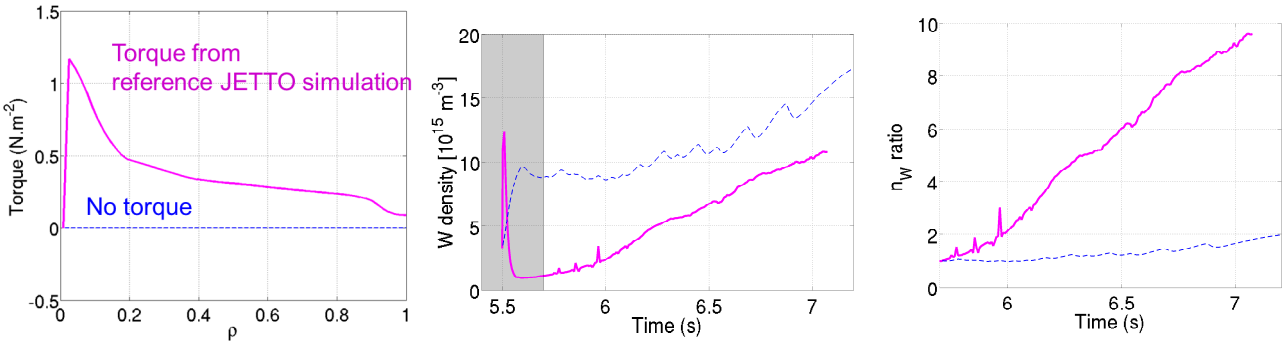

(a) NBI torque profile at t=6.5s. (b) W density over time at ρ=0.1. (c) W density ratio $\frac{n_W}{n_W(\tau_E}$ over time

Figure 20: Study of the impact of toroidal velocity on W accumulation. Reference simulation (magenta) versus simulation with toroidal rotation at zero (blue)

On figure 20b, during the first confinement time in the shaded area, for the reference simulation in magenta, the central W content drops before increasing again. Indeed W density profile equilibration time scale is much shorter than the energy confinement time scale. The removal of the NBI angular momentum makes the W transport much more sensitive to the initial condition. However, for the simulation with no torque, the W content remains stable and then increases. This makes the two simulations not directly comparable. In order to remove the effect of the first confinement time on W density, figure 20c shows the timetrace of W density normalized to its value at the end of the first confinement time, at t=5.7s. Without NBI angular momentum, W central content doubles over time, while in presence of toroidal rotation, the W density increases by a factor 10. This clearly illustrates that the toroidal rotation plays a role in the W central accumulation process.

The removal of the toroidal rotation causes the two simulations to have very different early phases and therefore completely different time evolutions. We shall focus on the first confinement time in order to understand the mechanisms leading to such a big difference.

As mentioned earlier, the initial W density profile is homothetic to the electron density profile, therefore some W is already present in the center at the start. In absence of toroidal rotation, the W is equally poloidally distributed along each flux surface which reduces significantly its neoclassical inward convection. Figure 21 shows the W transport coefficients at the end of the first confinement time, at t=5.7s, time averaged over 0.1s to smooth the QuaLiKiz predictions.

As expected, the removal of the rotation reduces by a factor P_A, the neoclassical diffusion and convection (on figure 21c and 21d). The neoclassical convection is strongly

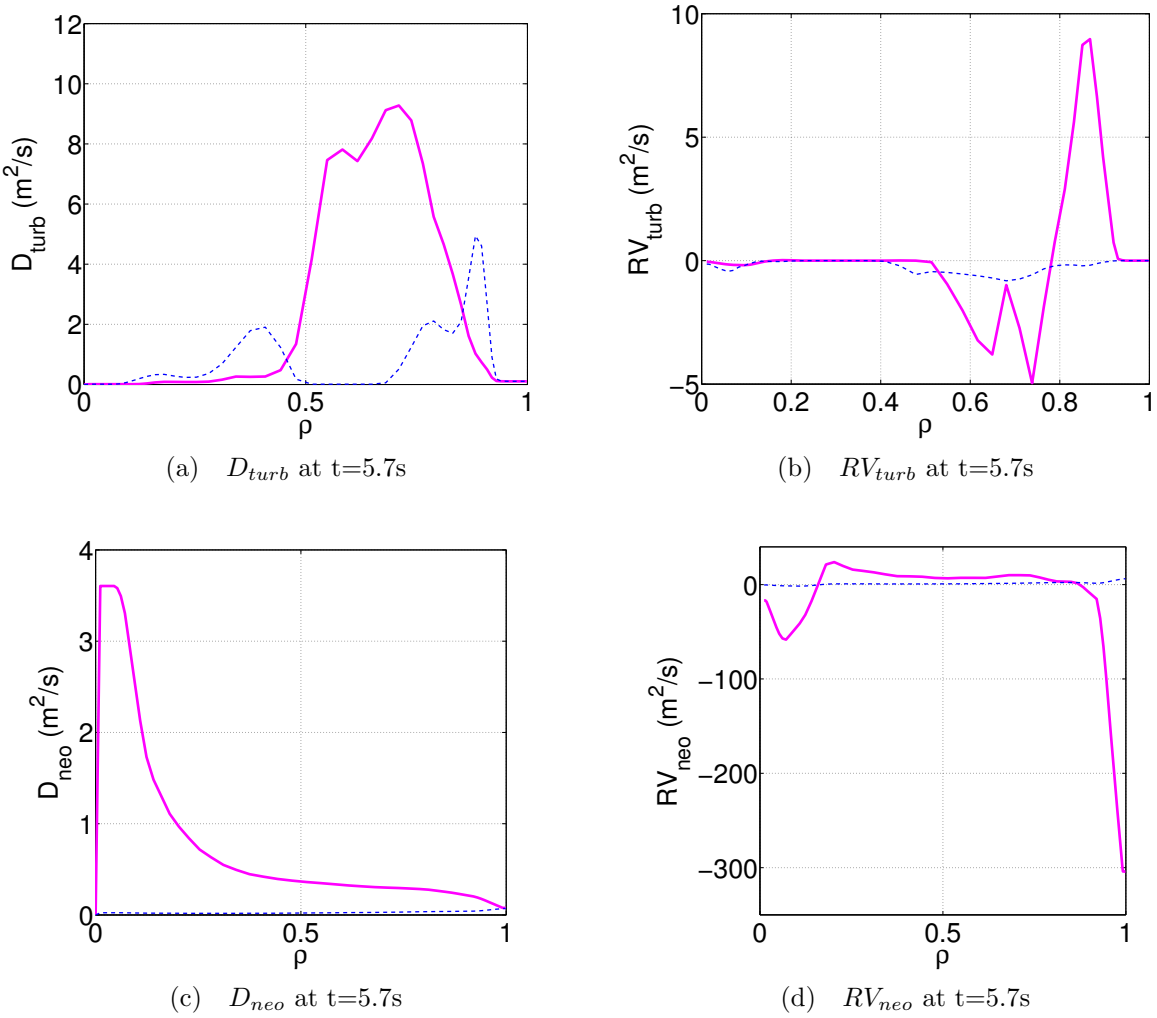

(a) D_{turb} at t=5.7s

(b) RV_{turb} at t=5.7s

(c) D_{neo} at t=5.7s

(d) RV_{neo} at t=5.7s

Figure 21: W transport coefficients at t=5.7s, time averaged over 0.1s. Reference simulation (magenta), no toroidal rotation (blue)

reduced both in the very core and in the pedestal region.

The absence of rotation also reduces the turbulent convection and diffusion for $\rho > 0.5$ by up to a factor 10. The impact of poloidal asymmetries on W turbulent transport is accounted for in QuaLiKiz based on [31], as described in [15]. The impact of centrifugal effects on the various components of the turbulent convection (thermodiffusion, rotodiffusion, pure convection) results of a complex compensation of the different components (see [31]) leading, in this case, to a reduced turbulent W transport in absence of rotation.

Overall, in absence of rotation, both turbulent and neoclassical W transport are reduced. As a consequence, W is no longer flushed out from the central zone of the plasma in the first confinement time. During the rest of the simulation, it is weakly transported to the center by residual neoclassical convection, but the W amount transported is negligible compared with the case with rotation (see figure 20c).

When removing the toroidal rotation, the turbulent main ions heat and particle fluxes are also affected. Figure 22 shows the heat fluxes profiles from JETTO simulations (reference and without rotation) at t=5.7s, after the first confinement time. When setting to zero the toroidal rotation, the $E \times B$ shear is largely reduced [32]. Due to a weaker $E \times B$ shear, the heat coefficients are larger in absence of rotation. As a consequence, the electron and ion temperatures are larger in absence of rotation, as seen on figures 23b and 23c. Note that the electron density profile on figure 23a is weakly impacted, except for the central density peaking which is slightly higher in absence of rotation. The central radiation on figure 23d is larger in absence of rotation since the W is not flushed out.

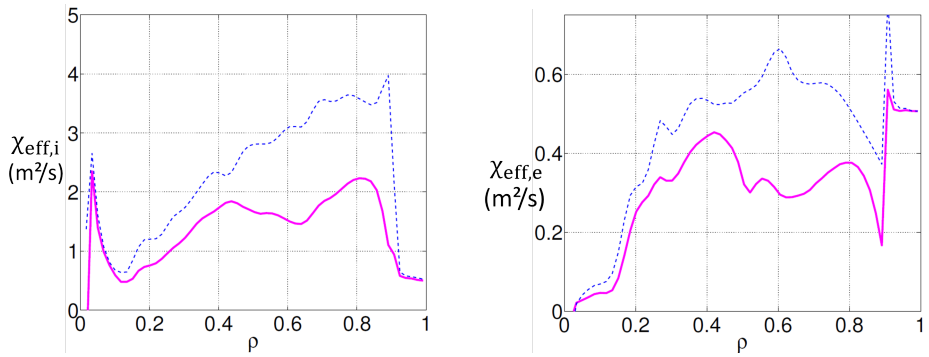

(a) JETTO ion heat effective diffusivity profile at t=5.7s

(b) JETTO electron heat effective diffusivity profile at t=5.7s

Figure 22: Ion and electron heat effective diffusivities profiles from JETTO simulations at t=5.7s : reference (magenta) and without rotation (blue).

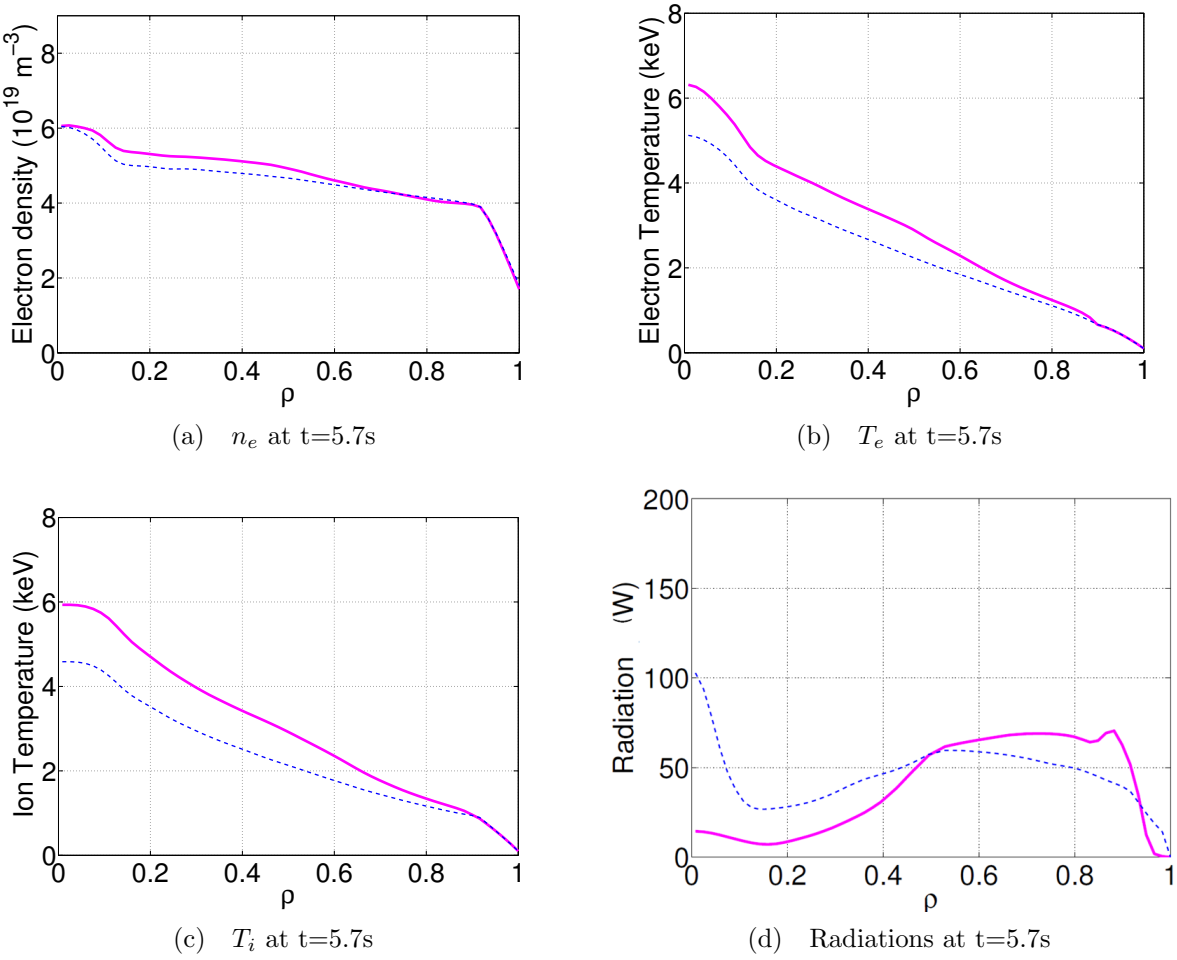

(a) n_e at t=5.7s

(b) T_e at t=5.7s

(c) T_i at t=5.7s

(d) Radiations at t=5.7s

Figure 23: Density, temperatures and radiation profiles at t=5.7s. Reference simulation (magenta), no toroidal rotation (blue)

In summary, the removal of the toroidal rotation strongly reduce the W neoclassical convection, as expected, and also its turbulent transport (see figure 21). But removing the rotation leads to more unstable background plasma heat and particle transport (see figures 22a and 22b). Initially, the removal of the rotation is deleterious for both the energy confinement (increased turbulence for main ion and electrons) and the central W content since W is no longer flushed out. But once the impact of the initial condition removed, it appears that toroidal rotation has a negative impact on the W central accumulation (see figure 20c). Therefore lower torque experiments, such as WEST or ITER, should be less prone to core W accumulation.

6. Non-linearities : W stabilization impact

A simulation evolving self-consistently particle, heat, momentum for electrons, ions and impurities (W and Be) involves numerous non-linearities. One of these features is illustrated by the fact that removing the W from our reference simulation leads to a

slightly lower total energy content, see figure 24d. In the simulation with Be only, the Z_{eff} is still 1.34 as in the reference simulation, except that Be is the only impurity. When removing the W while keeping Z_{eff} constant, the lower energy content is explained by a higher ion heat effective diffusivity, see figure 24a, while maintaining similar electron heat and ion particle effective diffusivities, see figures 24b and 24c.

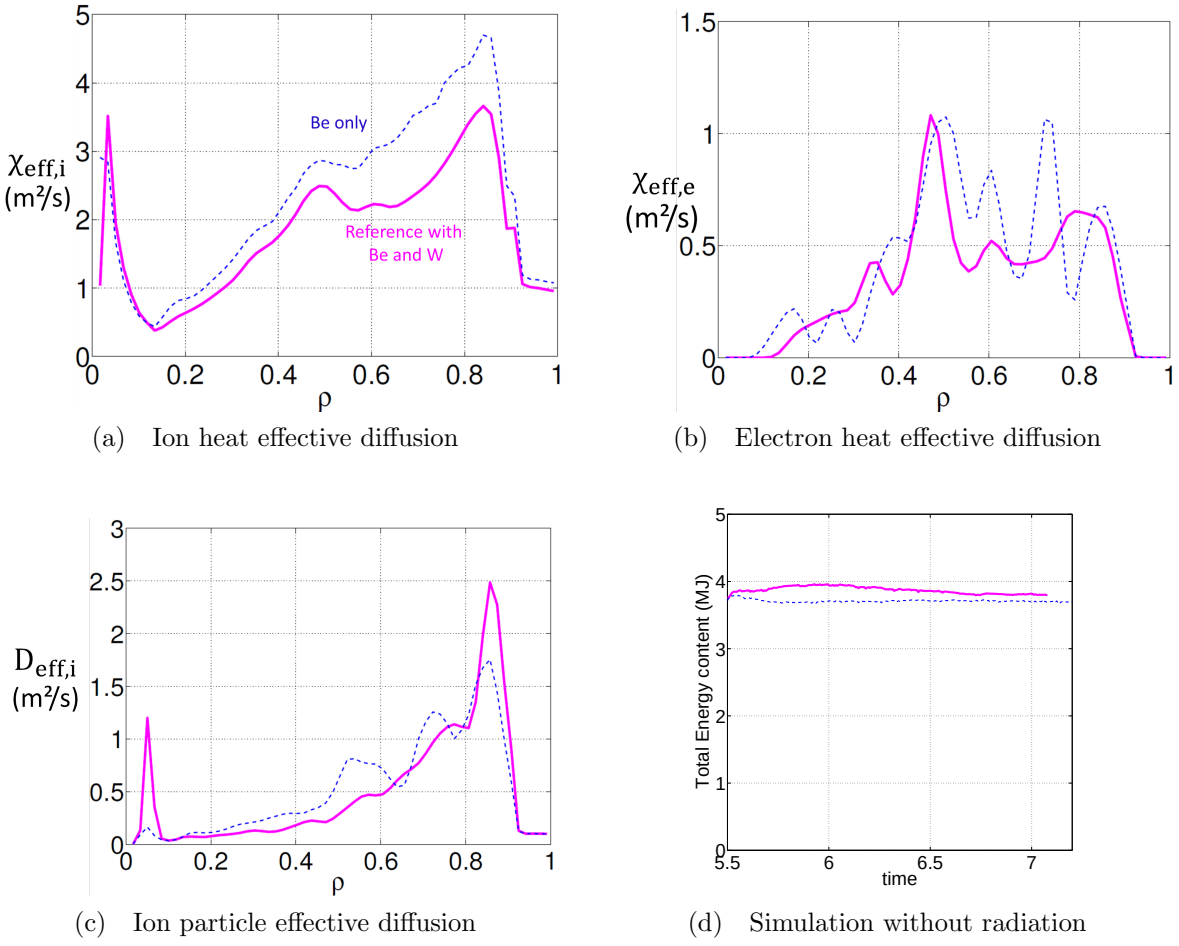

(a) Ion heat effective diffusion

(b) Electron heat effective diffusion

(c) Ion particle effective diffusion

(d) Simulation without radiation

Figure 24: Ion and electron heat effective diffusion and ion particle effective diffusion profiles at t=6.5s, and timetrace of the total energy content. Reference simulation with W and Be (magenta) and simulation with Be only (blue)

Removing the W from our reference simulation impacts the radiation level, the plasma collisionality and the plasma dilution.

6.1. Possible cause : radiation

When removing the W from our reference simulation the radiation level is almost reduced to zero. Therefore to isolate the impact of radiation from the impact of the W itself, a simulation as our refernce case but with the radiation forced to zero is run.

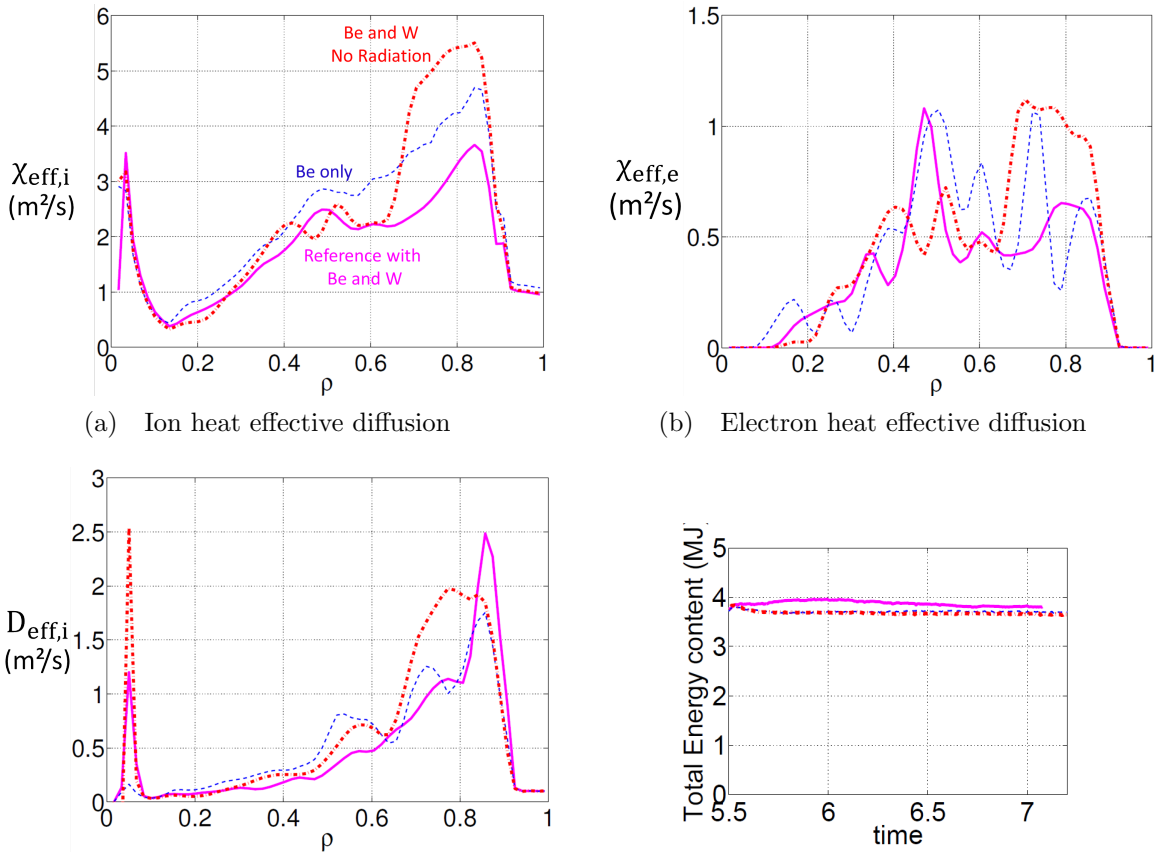

(a) Ion heat effective diffusion

(b) Electron heat effective diffusion

(c) Ion particle effective diffusion

(d) Simulation without radiation

Figure 25: Ion and electron heat effective diffusion and ion particle effective diffusion at t=6.5s, and timetrace of the total energy content. Reference simulation with W and Be (magenta),simulation with Be only (blue) and simulation with Be and W without radiation (red)

It is interesting to note that the energy content of the Be only case and W-Be but no radiation case are very similar (within 1%), see figure 25d. When comparing the effective ion heat diffusivities, removing the radiation from the reference case is destabilizing for $\rho > 0.6$, see figure 25a. A similar impact is seen also on the electron heat effective diffusivity, figure 25b, as well as on the ion particle effective diffusivity, figure 25c.

In order to have a better understanding of the stabilization effect, the timetraces of ion and electron temperatures, the ratio T_e/T_i and the ion heat diffusivity are shown on figure 26 for the position ρ=0.7.

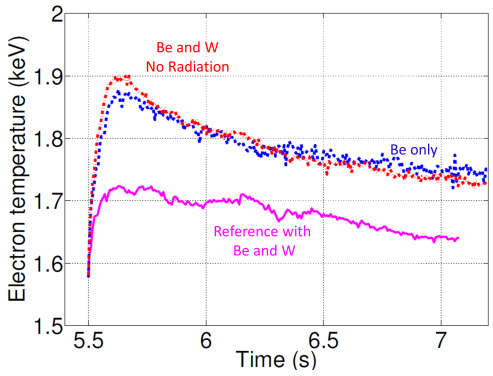

(a) Electron temperature

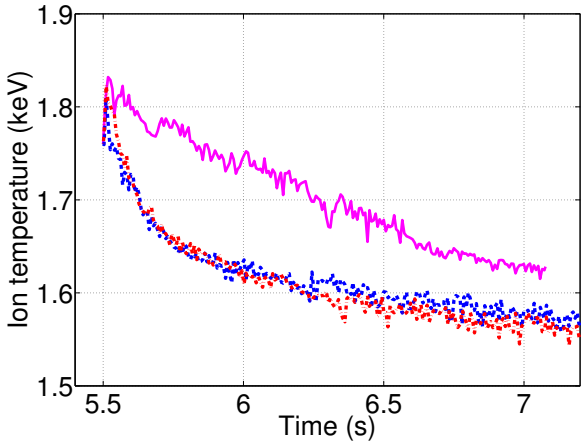

(b) Ion temperature

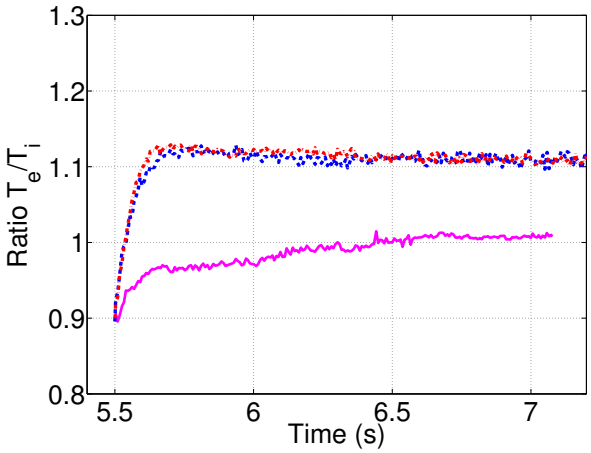

(c) Ratio T_e/T_i

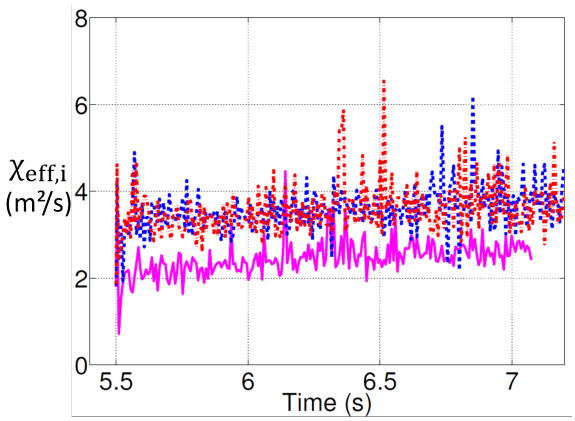

(d) Ion heat eff. diff.

Figure 26: Ion and electron temperatures, ratio T_e/T_i and ion heat effective diffusion timetraces at ρ=0.7. Reference simulation with W and Be (magenta), simulation with Be only (blue) and simulation with Be and W without radiation (red)

The curves split in two groups : the reference simulation with W and radiation on one side (magenta), and the simulations without radiation either with or without W on the other side. Without radiation, as expected, the electron temperature on figure 26a is higher. The ion temperature on figure 26b is also impacted and is lowered in absence of W or in absence of radiation. The modification in the temperature impacts the ratio T_e/T_i shown on figure 26c, which is higher for the simulations without W and without radiation.

The enhanced electron temperature, combined with lower ion temperature leads to enhanced T_e/T_i, which is known to increase turbulence [21]. Therefore, the stabilization effect could be explained by this mechanism : the removal of W causes the radiation level to be significantly reduced, leading to an enhanced T_e/T_i, causing the turbulence to be reduced. In order to validate this explanation, a QuaLiKiz standalone simulation

is run, scanning the electron temperature. All the other inputs are taken from the JETTO reference simulation parameters from t=6.5s and ρ=0.7. The ion and electron heat effective diffusivities and the ion particle effective diffusion are shown on figure 27. The red diamond corresponds to the T_e/T_i ratio at t=5.7s at ρ=0.7 for the simulation without radiation, in red on figure 26. The magenta circle corresponds to the T_e/T_i ratio at t=5.7s and at ρ=0.7 for the reference simulation. Note that JETTO is an iterative flux driven process while in QuaLiKiz standalone the gradients are kept fixed.

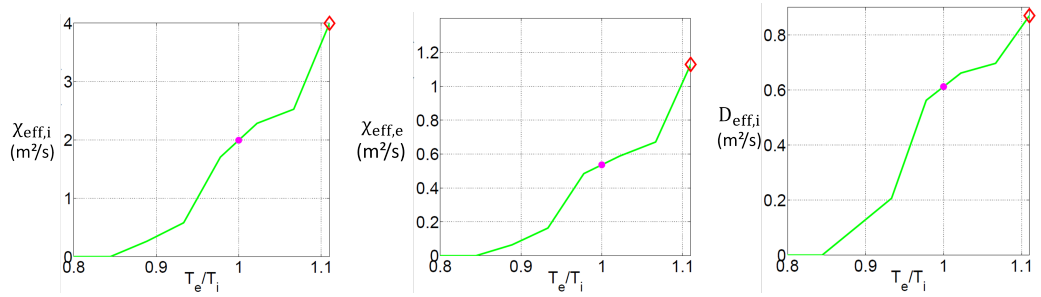

(a) Ion heat effective diffusion (b) Electron heat effective diffusion (c) Ion particle effective diffusion

Figure 27: QuaLiKiz standalone : ion and electron heat effective diffusion and ion particle effective diffusion at t=6.5s.

On figure 27a and 27b, ion and electron heat effective diffusivities both increase with the ratio T_e/T_i, as expected. It is coherent with the JETTO simulation, figure 26. Note that the slope of the increase of heat coefficients is quite stiff. As a consequence, a small modification of the T_e/T_i ratio impacts significantly the turbulence. In this case, the removal of the radiation (i.e. the variation of heat diffusion between the red diamond and the magenta circle) caused an increase of 2.0 m^2/s for the ion heat diffusion, 0.54 m^2/s for the electron heat coefficient and 0.61 m^2/s for the ion particle diffusion coefficient.

The removal of the radiation impacts the temperature and has a destabilizing effect. This indicates that a significant portion of the stabilization phenomenon occurs through the radiation. The next section focuses on the other mechanism susceptible to has a stabilizing effect : the combined effect of dilution and increased collisionality.

6.2. Other possible cause: dilution and increased collisionality

The other mechanism that could participate to the stabilization effect of W, is the combination of dilution and increased collisionality. Indeed, even if W is a trace impurity, it undergoes poloidal asymmetries and therefore can locally no longer be a trace species. Figure 28 shows the 2D poloidal cut of the W contribution to the Z_{eff} at t=6.5s as an illustration. The W contribution to Z_{eff} remains similar at all times of the simulation.

On the LFS the poloidal asymmetries cause the W to contribute to Z_{eff} up to 0.5. In those zones, the W is no longer a trace species and can contribute to the main ion

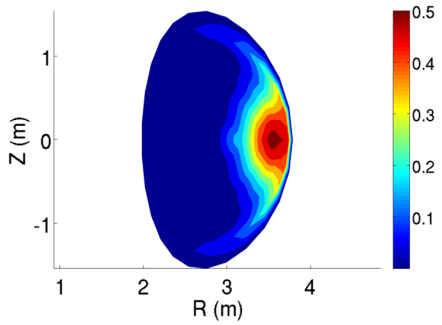

Figure 28: W contribution to the effective charge $\Delta Z_{eff} = Z^2 n_W / n_e$ at t=6.5s

dilution as well as modify the collisionality. Since the interchange ITG-TEM modes are ballooned on the low field side, where the W contribution to Z_{eff} is maximal it can indeed loaclly stabilize the turbulence through dilution [33, 34, 35, 21]. Moreover, W locally contributes to collisions, causing electrons to be untrapped and therefore lowering the TEM contribution. Both those effects caused by W can stabilize turbulence.

Using QuaLiKiz in stand-alone, the W concentration is increased and its impact on the effective diffusivities is illustrated by figure 29. The blue star corresponds to the zero W concentration for the simulation with Be only, in blue on figures 25. The magenta circle corresponds to the W concentration at t=6.5s at ρ=0.7 for the reference simulation.

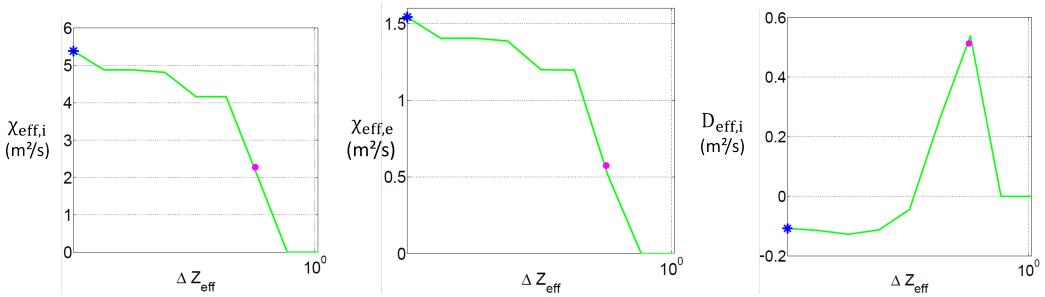

(a) Ion heat effective diffusion (b) Electron heat effective diffusion (c) Ion particle effective diffusion

Figure 29: QuaLiKiz standalone : ion and electron heat effective diffusion and ion particle effective diffusion at t=6.5s.

On figure 29a and 29b, ion and electron heat effective diffusivities remain unchanged until they reach a ΔZ_{eff} of $\simeq$ 0.3. On figure 29c, the main ion particle effective diffusivity follows a different trend, as it includes both the convective and diffusive contributions. The values of transport coefficients between the case without W and the W concentration from reference JETTO simulation (ie the difference between the blue star and the magenta circle) are of 3.1 m^2/s for the ion heat diffusion, 0.97 m^2/s for the electron heat coefficient and 0.62 m^2/s for the ion particle diffusion coefficient. Therefore

the contribution of the dilution to the stabilization effect is 30% bigger compared with the contribution through the radiation seen on figures 27.

Overall, the W has a stabilizing effect on the turbulence. The effect occurs through radiation and the modification of temperature profiles, but also through main ion dilution and increase of collisionality.

7. Conclusions and outlook

Overall, for the first time, an integrated, flux driven, modeling, evolving 7 channels (current, temperature, main ion Be and W densities and rotation profiles) over multiple confinement times was performed. Within the integrated modeling environment JETTO, first-principles codes such as QuaLiKiz and NEO model respectively turbulent and neoclassical transport, up to the pedestal top. An empirical model is tuned to reproduce experimental measurements in the pedestal. The NBI particle, heat and sources are self-consistently modeled using PENCIL, while SANCO evolves the radiation levels.

The simulation successfully reproduces the time evolution over 1.5s (hence 5 confinement times) of the temperature, density and rotation profiles. Moreover, the W central accumulation is captured with the simulation of turbulent and neoclassical transport, while keeping a constant W influx at the separatrix over time.

Actuators of the W accumulation are studied. It appears that removing the central NBI particle source cancels the central W accumulation, and cutting by half the central particle fuelling reduces also by half the W central accumulation. The suppression of the torque reduces the neoclassical W transport as expected, but also reduces the W turbulent transport. In this case, switching off the toroidal rotation has a destabilizing impact on the main ion and electron turbulence, and a stabilizing impact on the W transport. Therefore the W remains in the plasma center, however the accumulation is weaker. This is encouraging for devices such as WEST or ITER, which will operate without external torque, and without central particle fuelling.

Finally, it is observed that the presence of W has a stabilizing impact and leads to slightly higher energy content. Indeed, through radiation, the presence of W leads to lower T_e/T_i which is stabilizing ITG turbulence. This mechanism represents most of the stabilization effect. Moreover, on the low field side, because of W poloidal asymmetries in a rotating plasma, the W contribution to Z_{eff} at the outboard mid-plane can go up to 0.5. This Z_{eff} increment is also stabilizing the ITG turbulence. Nonetheless, these interesting impact of W on the confinement are not sufficient to compensate for the deleterious impact of W accumulation.

8. Acknowledgments

This work has been carried out within the framework of the EUROfusion Consortium and has received funding from the Euratom research and training programme 2014-

2018 under grant agreement No 633053. The views and opinions expressed herein do not necessarily reflect those of the European Commission.

9. Appendix

9.1. JETTO numerical settings

JETTO settings :	Shot Number	82722
	Number of grid points	61
	Start time (s)	45.5
	End time (s)	47.1
	Minimum timestep (s)	10^{-8}
	Maximum timestep (s)	10^{-3}
	Ion (1) mass	2
	Current boundary condition (amps)	$1.67.10^{6}$
	Electron temperature boundary condition (eV)	10^{2}
	Ion temperature boundary condition (eV)	10^{2}
	Ion Density boundary condition (cm^{-3})	$1.5.10^{13}$
	Edge velocity boundary condition (cm/s)	10^{6}
	grid resolution for QuaLiKiz	25

SANCO settings :

	Tungsten	Berylium
Impurity mass	184	9.0129
Impurity charge	74	4
Escape velocity (cm/s)	0	0
Neutral flux (s^{-1})	10^{15}	10^{14}
Recycling factor	0	0
Abundance	1	300
ratio SANCO/JETTO timestep	100	100

NEO settings :	Radial grid	16
	Pitch angle polynomials	13
	NEO transport update timestep (s)	2.10^{-4}

QuaLiKiz settings :

ρ_{min}	
ρ_{max}	
impact of $U_{\|\|}$, $\nabla U_{\|\|}$ and $E \times B$	
$k_\theta \rho$ range	I
added diffusion coefficient to ensure numerical stability	a Bohm diffusion of 0.1% of the particle diffu

ETB settings :	Pedestal width (cm)	4
	Lower Thermal limit (cm^2/s)	5.10^3
	Lower particle ion limit (cm^2/s)	1.10^3
	Top Of Barrier FRANTIC gas puff target (cm^{-3})	$4.5.10^{13}$
	Top Of Barrier FRANTIC ion nominal puff rate (s^{-1})	6.10^{21}
	FRANTIC recycling coefficient	0.1
	ELM model max. transport multiplier (m^2/s)	1.10^8
	Prandtl number for ETB	0.75

PENCIL settings :

	Octant 4	Octant 8
Ion Mass	2	2
Ion energy (keV)	90	97
Beam fraction with E, E/2, E/3	0.51, 0.28, 0.21	0.52, 0.30, 0.18
Pini's	1, 4, 6	1, 4, 6
Normalize power to (MW)	6	10

Acknowledgments

This work has been carried out within the framework of the EUROfusion Consortium and has received funding from the Euratom research and training programme 2014-2018 under grant agreement No 633053. The views and opinions expressed herein do not necessarily reflect those of the European Commission.

References

[1] GF Matthews, M Beurskens, S Brezinsek, M Groth, et al. "JET ITER-like walloverview and experimental programme". In: *Physica Scripta* 2011.T145 (2011), p. 014001.

[2] S. P. Hirshman and D.J. Sigmar. "Neoclassical transport of impurities in tokamak plasmas". In: *Nucl. Fusion* 1079 (1981).

[3] P. Helander and D.J. Sigmar. *Collisional Transport in Magnetized Plasmas*. 2002.

[4] C. Angioni, L. Carraro, T. Dannert, N. Dubuit, et al. "Particle and impurity transport in the Axial Symmetric Divertor Experiment Upgrade and the Joint European Torus, experimental observations and theoretical understanding". In: *Physics of Plasmas* 14.5 (2007), pp. 1–9. ISSN: 1070664X.

[5] T. Fülöp, S. Braun, and I. Pusztai. "Impurity transport driven by ion temperature gradient turbulence in tokamak plasmas". In: *Physics of Plasmas* 17.6 (2010), pp. 1–9. ISSN: 1070664X.

[6] C Angioni, P Mantica, T Pütterich, M Valisa, et al. "Tungsten transport in JET H-mode plasmas in hybrid scenario, experimental observations and modelling". In: *Nuclear Fusion* 54.8 (2014), p. 83028.

[7] Michele Romanelli, Gerard Corrigan, Vassili Parail, Sven Wiesen, et al. "JINTRAC : A System of Codes for Integrated Simulation of". In: *Plasma and Fusion Research* 9 (2014), pp. 1–4.

[8] A Loarte, ML Reinke, AR Polevoi, M Hosokawa, et al. "Tungsten impurity transport experiments in Alcator C-Mod to address high priority research and development for ITER a". In: *Physics of Plasmas* 22.5 (2015), p. 056117.

[9] N Fedorczak, P Monier-Garbet, T Pütterich, S Brezinsek, et al. "Tungsten transport and sources control in JET ITER-like wall H-mode plasmas". In: *Journal of nuclear materials* 463 (2015), pp. 85–90.

[10] A. G. Peeters, Y. Camenen, F. J. Casson, W. A. Hornsby, et al. "The nonlinear gyro-kinetic flux tube code GKW". English. In: *Computer Physics Communications* 180.12 (2009), 2650–2672. ISSN: 0010-4655.

[11] E A Belli and J Candy. "Drift-Kinetic Simulations of Neoclassical Transport APS-DPP Meeting Motivation for the NEO code". In: (2008).

[12] E A Belli and J Candy. "Full linearized FokkerPlanck collisions in neoclassical transport simulations". In: *Plasma Phys. Control. Fusion* 54.54 (2012), pp. 15015–17. ISSN: 0741-3335.

[13] C Bourdelle, X Garbet, F Imbeaux, A Casati, et al. "A new gyrokinetic quasilinear transport model applied to particle transport in tokamak plasmas". In: *Physics of Plasmas* 14.11 (2007), p. 112501.

[14] C Bourdelle, J Citrin, B Baiocchi, A Casati, et al. "Core turbulent transport in tokamak plasmas: bridging theory and experiment with QuaLiKiz". In: *Plasma Physics and Controlled Fusion* 58.1 (2016), p. 014036.

[15] Jonathan Citrin, Clarisse Bourdelle, Francis J Casson, Clemente Angioni, et al. "Tractable flux-driven temperature, density, and rotation profile evolution with the quasilinear gyrokinetic transport model QuaLiKiz". In: *Plasma Physics and Controlled Fusion* (2017).

[16] L. Lauro-Taroni et al. "Impurity Transport of High Performance Discharges in JET". In: *Proc. 21st EPS* 1.102 (1994).

[17] P Mantica, C Angioni, L Lauro Taroni, M Valisa, et al. "Transport analysis of Tungsten and Beryllium in JET Hybrid Plasmas with the ITER-like wall". In: 577.1997 (2012), p. 2012.

[18] M Sertoli, T Odstrcil, C Angioni, et al. "Interplay between central ECRH and saturated (m, n)=(1, 1) MHD activity in mitigating tungsten accumulation at ASDEX Upgrade". In: *Nuclear Fusion* 55.11 (2015), p. 113029.

[19] G Cenacchi and A Taroni. *JET Internal Report*. 1988.

[20] CD Challis, JG Cordey, H Hamnen, PM Stubberfield, et al. "Non-inductively driven currents in JET". In: *Nuclear Fusion* 29.4 (1989), p. 563.

[21] A Casati, C Bourdelle, X Garbet, F Imbeaux, et al. "Validating a quasi-linear transport model versus nonlinear simulations". In: *Nuclear Fusion* 49.8 (2009), p. 085012.

[22] J. Citrin, C. Bourdelle, P. Cottier, D. F. Escande, et al. "Quasilinear transport modelling at low magnetic shear". In: *Physics of Plasmas* 19.6 (2012). ISSN: 1070664X.

[23] S. Tamor. "ANTIC : A Code for Calculation of Neutral Transport in Cylindrical Plasmas". In: 19 (1980).

[24] Florian Koechl, Alberto Loarte, Vassili Parail, Paula Belo, et al. "Modelling of transitions between L-and H-mode in JET high plasma current plasmas and application to ITER scenarios including tungsten behaviour". In: *Nuclear Fusion* (2017).

[25] LL Lao, H St John, RD Stambaugh, AG Kellman, and W Pfeiffer. "Reconstruction of current profile parameters and plasma shapes in tokamaks". In: *Nuclear fusion* 25.11 (1985), p. 1611.

[26] M Gelfusa, A Murari, I Lupelli, N Hawkes, et al. "Influence of plasma diagnostics and constraints on the quality of equilibrium reconstructions on Joint European Torus". In: *Review of Scientific Instruments* 84.10 (2013), p. 103508.

[27] Th Pütterich, R Neu, R Dux, AD Whiteford, MG O'Mullane, HP Summers, et al. "Calculation and experimental test of the cooling factor of tungsten". In: *Nuclear Fusion* 50.2 (2010), p. 025012.

[28] Alexei Pankin, Douglas McCune, Robert Andre, Glenn Bateman, and Arnold Kritz. "The tokamak Monte Carlo fast ion module NUBEAM in the National Transport Code Collaboration library". In: *Computer Physics Communications* 159.3 (2004), pp. 157–184.

[29] C. Angioni, F. J. Casson, P. Mantica, T. Pütterich, et al. "The impact of poloidal asymmetries on tungsten transport in the core of JET H-mode plasmas". In: *Physics of Plasmas* 22.5 (2015). ISSN: 10897674.

[30] S. Breton, F. J. Casson, C. Bourdelle, C. Angioni, et al. "High Z neoclassical transport: Application and limitation of analytical formulae for modelling JET experimental parameters". In: *Physics of Plasmas* 25.1 (2018), p. 012303. eprint: https://doi.org/10.1063/1.5019275.

[31] C Angioni, FJ Casson, C Veth, and AG Peeters. "Analytic formulae for centrifugal effects on turbulent transport of trace impurities in tokamak plasmas". In: *Physics of Plasmas* 19.12 (2012), p. 122311.

[32] Taik Soo Hahm and Keith H Burrell. "Role of flow shear in enhanced core confinement regimes". In: *Plasma Physics and Controlled Fusion* 38.8 (1996), p. 1427.

[33] RR Dominguez and MN Rosenbluth. "Local kinetic stability analysis of the ion temperature gradient mode". In: *Nuclear fusion* 29.5 (1989), p. 844.

[34] GM Staebler, GL Jackson, WP West, SL Allen, et al. "Improved High-Confinement Mode with Neon Injection in the DIII-D Tokamak". In: *Physical review letters* 82.8 (1999), p. 1692.

[35] C Bourdelle, X Garbet, GT Hoang, J Ongena, and RV Budny. "Stability analysis of improved confinement discharges: internal transport barriers in Tore Supra and radiative improved mode in TEXTOR". In: *Nuclear Fusion* 42.7 (2002), p. 892.

[36] M Erba, A Cherubini, VV Parail, E Springmann, and A Taroni. "Development of a non-local model for tokamak heat transport in L-mode, H-mode and transient regimes". In: *Plasma Physics and Controlled Fusion* 39.2 (1997), p. 261.